An automated approach to quasi-periodic noise removal in natural images

Frédéric Sur, Michel Grediac

▶ **To cite this version:**

Frédéric Sur, Michel Grediac. An automated approach to quasi-periodic noise removal in natural images. [Research Report] RR-8660, INRIA Nancy, équipe Magrit; Institut Pascal, Université Blaise Pascal; INRIA. 2015. hal-01099795

HAL Id: hal-01099795
https://inria.hal.science/hal-01099795

Submitted on 5 Jan 2015

HAL is a multi-disciplinary open access archive for the deposit and dissemination of scientific research documents, whether they are published or not. The documents may come from teaching and research institutions in France or abroad, or from public or private research centers.

L'archive ouverte pluridisciplinaire **HAL**, est destinée au dépôt et à la diffusion de documents scientifiques de niveau recherche, publiés ou non, émanant des établissements d'enseignement et de recherche français ou étrangers, des laboratoires publics ou privés.

An Automated Approach to Quasi-Periodic Noise Removal in Natural Images

Frédéric SUR, **Michel** GRÉDIAC

RESEARCH REPORT

N° 8660

Jan. 2015

Project-Team Magrit & Institut Pascal (Clermont Université)

ISSN 0249-6399 ISRN INRIA/RR--8660--FR+ENG

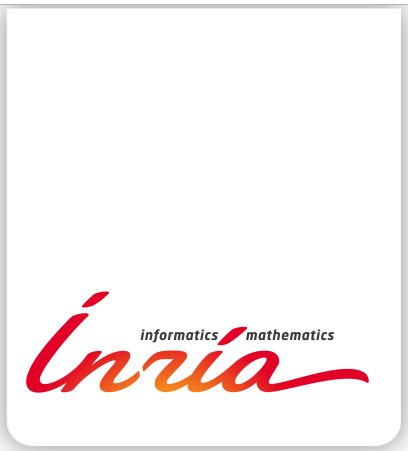

An Automated Approach to Quasi-Periodic Noise Removal in Natural Images

Frédéric Sur*, Michel Grédiac†

Project-Team Magrit & Institut Pascal (Clermont Université)

Research Report n° 8660 — Jan. 2015 — 57 pages

Abstract: Quasi-periodic noise may affect digital images. This phenomenon is reflected by spurious repetitive patterns covering the whole image. Quasi-periodic noise is by nature well localized in the Fourier spectrum. A possibility is thus to attenuate it through a well-designed notch filter. In contrast to existing algorithms which require hand-tuned filter design, this research report presents an automated approach based on the expected power spectrum of a natural image. The resulting algorithm enables to eliminate a large range of repetitive structures, from simple periodic noises, whose influence on the image spectrum is limited to a few Fourier coefficients, to quasi-periodic noises with much more complex spectrum structures. The proposed algorithm is assessed on the basis of various experiments. A comparison with morphological component analysis (MCA), a blind source separation algorithm, is also provided. A Matlab implementation is available. This report is an extension of a published article.

Key-words: quasi-periodic noise, power spectrum distribution, notch filter design

* LORIA Umr 7503 - projet Magrit, Université de Lorraine, Cnrs, Inria, Campus Scientifique BP 239, 54506 Vandœuvre-lès-Nancy cedex, France.

† Institut Pascal Umr Cnrs 6602, Université Blaise Pascal BP 10448, 63000 Clermont-Ferrand, France

RESEARCH CENTRE NANCY – GRAND EST

615 rue du Jardin Botanique
CS20101
54603 Villers-lès-Nancy Cedex

Une approche automatisée pour l'élimination du bruit quasi-périodique dans les images naturelles

Résumé : Les images numériques sont susceptibles d'être affectées par un bruit quasi-périodique. Ce phénomène se manifeste par des motifs répétés parasites couvrant la totalité de l'image. Le bruit quasi-périodique est par nature bien localisé dans le domaine de Fourier. Il est donc possible de l'atténuer par l'intermédiaire d'un filtre coupe-bande. À la différence des algorithmes existants qui nécessitent une modélisation du filtre ou un paramétrage manuels, ce rapport de recherche présente une approche automatisée basée sur le spectre de puissance moyen d'une image naturelle. L'algorithme résultant permet d'éliminer une grande variété de structures répétées, de simples bruits périodiques (dont la contribution au spectre de l'image est limitée à quelques coefficients de Fourier) à des bruits quasi-périodiques présentant des spectres de structure bien plus complexe. L'algorithme proposé est évalué sur de nombreuses expériences. Une comparaison avec l'analyse en composantes morphologiques (MCA), un algorithme de séparation aveugle de sources, est discutée. Une implémentation Matlab est également disponible. Ce rapport est la version étendue d'un article publié.

Mots-clés : bruit quasi-périodique, distribution du spectre de puissance, construction de filtres coupe-bande.

Contents

1 Introduction

Digital images may be affected by spurious repetitive (or at least structured) patterns covering the entire image. This unwanted feature is called quasi-periodic noise in the literature, since it is quasi-periodically distributed. The phenomenon may arise from electrical interferences during image acquisition, miscalibrated sensors, or missing data, causing, for instance, line dropout, striping, banding, or more complex background noise. Remote sensing applications are especially affected [21]. Particular reprographic techniques such as halftone printing, or cathode ray tube (CRT) monitors (which are affected by visible scanlines) are also likely to cause this phenomenon.

While white noise estimation and removal is the subject of a huge body of literature (see, e.g., recent review papers [17, 18]), it appears that quasi-periodic noise has been addressed by relatively few studies. The basic method has not changed since the dawn of image processing for robotic probe imaging [20]. Periodic noise gives more or less sharp spikes in the Fourier domain, which have to be filtered out through notch filters to remove the corresponding noisy patterns. A reminder of the available approaches can be found in [11]. The difficulty is to automate spike detection or, equivalently, notch filter design. Each Fourier coefficient indeed depends on the whole image content. Distinguishing between spikes caused by a localized texture or a repetitive structure (common in man-made environments) and spurious ones caused by periodic noise often requires prior knowledge. Some authors [1, 14] suggest detecting spikes in the Fourier domain as large deviations with respect to a localized median value. However, some parameters are still to be fixed by the user. It is important to mention that the efficient stripe removal approach described in a recent paper [9] is adapted to a subclass of stationary processes, namely convolved white noises. Even if periodic noise can be seen as a stationary process, it cannot be modeled as the convolution of a white noise with a simple kernel, therefore it is not within the scope of the paper in question.

Distinguishing between the underlying image and pseudo-periodic noise can also be seen as a blind source separation problem [28]. For instance, these two components can reasonably be assumed to be morphologically distinct in the sense of [8], that is, they have a sparse representation in two incoherent bases, one for the image component, the other for the periodic component. Ref. [23] provides some image decomposition examples using curvelet representation for the image component and DCT (discrete cosine transform) for the periodic component. However, a localized, high-frequency texture is likely to be represented in the periodic component, and consequently to be discarded with the periodic noise. The sparsity assumption is also debatable. This is discussed in the experimental assessment.

The proposed contribution is the automated design of a notch filter for pseudo-periodic noise removal, which is especially interesting for a blindly processing a series of images. It is based on the observation that, considering an image impaired by periodic noise, the sole periodic pattern present in every small patch extracted from this image is the periodic noise itself. An average power spectrum is thus calculated by averaging the power spectra of a set of patches from the noisy image. This basic idea is in fact not new and dates back to the nineteen-eighties. It was actually suggested in a short paper [4] and later applied to satellite image destriping [22]. We propose to systematize this approach and to consider spikes as deviations in a model of the expected average spectrum. It is indeed known [10, 19, 26, 27, 15] that the expected power spectrum of natural images can be modeled by a function which decreases with the inverse of some positive power of the frequency. Such a function should thus fit the average power spectrum, except at certain spikes, expected to be due to the noise pattern, which can subsequently be detected as statistical outliers.

The statistical background is explained in Sec. 2. The resulting algorithm is presented in Sec. 3, together with an illustrative example. Experiments are discussed in Sec. 4, and a com-

parison with morphological component analysis [8] (MCA) is provided. We conclude with Sec. 5.

This report is an extended version of [25].

A Matlab code is available here: `www.loria.fr/%7Esur/software/ARPENOS/`

2 Automated detection of spurious spikes caused by pseudo-periodic noise

We propose to detect the spikes in the Fourier domain by averaging power spectra over a set of patches covering the original image: the spikes in this average spectrum are likely to be caused by the periodic noise covering the whole image. After providing some notations in Sec. 2.1, a stochastic model of the average power spectrum is proposed in Sec. 2.2.

2.1 Reminder and notations

The discrete Fourier transform of an image i of size $X \times Y$ is defined as the $(X,Y)-$periodic function:

$$I(\xi,\eta) = \sum_{x=0}^{X-1}\sum_{y=0}^{Y-1} i(x,y)e^{-2\pi j(x\xi/X+y\eta/Y)} \tag{1}$$

where $j^2=-1$ and (ξ,η) have integer values. With $(\xi,\eta) \in [-X/2, X/2-1] \times [-Y/2, Y/2-1]$, $|I(\xi,\eta)|$ is the amplitude of a periodic component of frequencies ξ/X and η/Y (units are cycles per pixel) along each direction. $|I|$ is the amplitude spectrum of i and $|I|^2$ is the power spectrum of i. Since the pixel intensities $i(x,y)$ are real numbers, the (amplitude or power) spectrum is symmetric with respect to $(\xi,\eta)=(0,0)$.

Both these spectra are affected by image edges and textures. For example, a part of image i with a periodic texture gives large $|I(\xi,\eta)|$ with (ξ,η) corresponding to the frequencies of the texture.

We also recall that a periodized translation by a vector (t_x,t_y) of any image i amounts to a multiplication of $I(\xi,\eta)$ by $e^{2\pi j(t_x\xi/X+t_y\eta/Y)}$. The amplitude and power spectra are thus not affected by translations.

Let us finish with some notations used in the rest of the report. We note (f,ϕ) the polar coordinates of a frequency pair (ξ,η) where f $(=\sqrt{(\xi/X)^2+(\eta/Y)^2}$ if measured in cycles per pixel) is the radial distance from $(0,0)$ and ϕ is the counterclockwise angle from the ξ-axis. For any complex number z, $\overline{z}$ is the conjugate and $\mathrm{Re}(z)$ the real part. Fourier transforms are capitalized.

2.2 Stochastic modeling

We assume that a set of patches spanning the whole image of interest is available, each patch being affected by the underlying periodic noise and by additional white noise. The aim of this section is to argue that the average power spectrum enables the periodic noise component to be characterized. The patches are assumed to be realizations of the following observation model.

Definition 2.1 *A random patch p is the sum of the noise-free component p_0, the periodic noise n, and Gaussian white noise w, i.e.,*

$$p(x,y) = p_0(x,y) + n(x,y) + w(x,y) \tag{2}$$

where

- p_0 *is a stochastic image patch;*
- $n = \tau_{t_x,t_y}(n_0)$ *is the translation of a pattern* n_0 *(with possible mild variations, hence modeled itself as a random image of expectation* $E(n_0)$*) by a random displacement* (t_x, t_y) *uniformly distributed in* $[1, X] \times [1, Y]$*. Since* n_0 *is the periodic noise component,* $E(n_0)$ *is the inverse Fourier transform of a sparse map (that is, made of a few spikes);*
- w *is a Gaussian white noise of variance* $Var(w)$*;*
- *The aforementioned random variables are independent.*

The Fourier transform being linear, the same relation holds in the Fourier domain:

$$P(\xi,\eta) = P_0(\xi,\eta) + N(\xi,\eta) + W(\xi,\eta) \tag{3}$$

for any frequency pair (ξ, η). The power spectra therefore satisfy

$$\begin{aligned} |P(\xi,\eta)|^2 =& |P_0(\xi,\eta)|^2 + |N(\xi,\eta)|^2 + |W(\xi,\eta)|^2 \\ &+ 2\,\mathrm{Re}\left(P_0(\xi,\eta)\overline{N(\xi,\eta)} + W(\xi,\eta)\overline{N(\xi,\eta)} + P_0(\xi,\eta)\overline{W(\xi,\eta)}\right) \end{aligned} \tag{4}$$

Taking the expectation in (4), since the random variables are assumed independent, we obtain (mentions of (ξ, η) are skipped for brevity):

$$\begin{aligned} E(|P|^2) =& E(|P_0|^2) + E(|N|^2) + E(|W|^2) \\ &+ 2\,\mathrm{Re}\left(E(P_0)E(\overline{N}) + E(W)E(\overline{N}) + E(P_0)E(\overline{W})\right) \end{aligned} \tag{5}$$

From the definition in Sec. 2.1, $E(|W|^2) = XY\mathrm{Var}(w)$, $E(\overline{W}) = E(W) = E(w) = 0$, and, with the translation property, $E(\overline{N}) = E(\overline{N_0})E(e^{-2\pi j(t_x\xi/X + t_y\eta/Y)})$ and $|\overline{N}| = |\overline{N_0}|$. Consequently,

$$E(|P|^2) = E(|P_0|^2) + E(|N_0|^2) + XY\mathrm{Var}(w) + 2\mathrm{Re}\left(E(P_0)E(\overline{N_0})E(e^{-2\pi j(t_x\xi/X + t_y\eta/Y)})\right). \tag{6}$$

Since t_x (respectively t_y) is assumed to be uniformly distributed in $[0, X]$ (respectively $[0, Y]$), $E(e^{-2\pi j(t_x\xi/X + t_y\eta/Y)} = 0$. We conclude that:

$$E(|P|^2) = E(|P_0|^2) + E(|N_0|^2) + XY\mathrm{Var}(w) \tag{7}$$

The expected power spectrum of patch p thus comprises three components, namely:

1. The expected power spectrum of the noise-free patch p_0. A large body of literature has been dedicated to the modeling of the power spectrum of natural images (see, e.g., [10, 27]). This spectrum is known to be well modeled by a $1/f$ power law; that is, there exist positive real values α and A such that

$$E(|P_0(f,\phi)|^2) = \frac{A}{f^\alpha} \tag{8}$$

where f and ϕ are defined in Sec. 2.1. Most natural images have $\alpha \simeq 2$ (or $\alpha \simeq 1$ when considering the amplitude spectrum). More sophisticated models are available: in [19, 26] for example, it was observed that both A and α actually depend on the angle ϕ. We do not use such an advanced model in this report, and simply use the $1/f$ power law given by (8).

2. The expected power spectrum of the quasi-periodic noise component n_0. It mainly consists of a few spikes, or relatively small regions spread along these spikes.

3. The contribution of the white noise w, constant over the whole spectrum. This contribution is dominated by the first two components, especially for low and medium frequencies. It is however possible that it dominates the high frequencies because of the power law (first component) and the limited number of frequencies characterizing the quasi-periodic noise (second component).

Neglecting the white noise, we can see that the expected spectrum of the patches can essentially be modeled by the spikes caused by the pseudo-periodic noise, superimposed on the power law distribution. It turns out that this simplified model is realistic in all the images affected by pseudo-periodic noise that we have encountered.

Fitting the power law to the average power spectrum thus gives an estimation of the parameters A and α, with the periodic noise components being statistical outliers. Furthermore, a notch filter n_f for an image i affected by quasi-periodic noise can be built from the localization of these outliers in the Fourier domain. An estimation of the de-noised image is subsequently given by the inverse Fourier transform of $N_f I$ (or equivalently by the convolution of n_f and i). It should be noted that what we call "notch filter" does not remove a single (more accurately two because of the symmetry property) (ξ, η) frequency pair, but potentially removes the contributions to the image spectrum of a whole set of frequency pairs, all of them being outliers with respect to the expected spectrum. The following section gives an algorithm based on this idea to remove pseudo-periodic noise.

3 An automated algorithm to remove pseudo-periodic noise from natural images

The algorithm is described in Sec. 3.1, practical considerations are discussed in Sec. 3.2, and an illustrative example is detailed in Sec. 3.3.

3.1 Algorithm

Given an image i of size $X \times Y$ impaired by quasi-periodic noise, the proposed algorithm consists of the following steps.

1. Calculate the average power spectrum (denoted $\widetilde{|P|^2}$) obtained by averaging the power spectrum of patches of size $L \times L$ regularly distributed in the image.

2. Fit a power law distribution to the power spectrum as a function of the frequency f, i.e., find A and α such that
$$\log\left(\widetilde{|P|^2}(f)\right) = A - \alpha \log(f) \tag{9}$$
The fitting is obtained by robust linear regression (we use iteratively reweighted least squares) on the $(\log(f), I(f, \phi))$ scatter plot for f between f_0 and f_1 (to be specified) cycles per pixels. Robust regression gives consistent estimations which are not influenced by the spurious spikes due to pseudo-periodic noise. Least square estimation also gives the standard deviation σ of the residues.

3. Find the localization of upper outliers in the average power spectrum as frequency pairs (ξ, η) such that, under the common 3σ rule,

$$\frac{\log\left(\widetilde{|P|^2}(\xi,\eta)|\right) - (A - \alpha\log(f))}{\sigma} > 3 \tag{10}$$

This results in an outlier map M_o^p such that $M_o^p(\xi,\eta) = 1$ if an outlier is present at (ξ,η) in the average spectrum of the patches, and $= 0$ otherwise. Note that a false positive rate of 1% is expected under a Gaussian distribution. We restrict the outlier detection to frequencies $f > f_2$ (to be specified), since low frequencies do not correspond to repetitive patterns.

4. Resize the outlier map of size $L \times L$ to size $X \times Y$, giving a map M_o of the probable spurious spikes caused by quasi-periodic noise in the original image spectrum. Multiplying the initial image spectrum by $1 - M_o$ acts as a notch filter, eliminating the influence of the quasi-periodic noise.

5. Retrieve an estimation $\widehat{n}$ of the periodic noise component as the inverse Fourier transform of $M_o(\xi,\eta)I(\xi,\eta)$, and the estimated de-noised image $\widehat{i}$ as $i - \widehat{n}$ (i.e. the inverse transform of $(1 - M_o(\xi,\eta))I(\xi,\eta)$).

3.2 Practical considerations

The implementation details presented below do not play a crucial role in the good behavior of the algorithm, but are given in order to enable the algorithm to be recreated.

First, since most images have discontinuities between their left/right (respectively top/bottom) borders, their spectrum shows dominant straight lines along the horizontal (respectively vertical) axis. To reduce these boundary effects, we multiply the patches p by a 2D Hann window with the same width L as the patches, as in earlier works [4, 19, 27].

In Step 1, the definition of the patches must be stipulated. Regarding the distribution of the sample of non-correlated patches i, the absence of correlation is required to ensure the consistency of the sample mean estimator, hence patches with no or only limited overlapping. The size of the patches should be large enough to ensure both a good accuracy in the periodic noise spike detection (frequencies are distributed with $1/L$ steps in the power spectrum of a patch, cf Sec. 2.1) and the detectability of low-frequency noise, but not too large, so as to make it possible to build enough independent patches from the noisy image of interest. Using $L \times L$ patches, we found that a good compromise is to take a sampling step of $L/8$ in both the horizontal and vertical directions, which gives a total number of patches equal to

$$\lceil 8(X - L)/L \rceil \times \lceil 8(Y - L)/L \rceil \tag{11}$$

with $\lceil \cdot \rceil$ rounding a number to the next larger integer. In addition, the average power spectrum is obtained by a geometric mean instead of an arithmetic mean, in order to limit the influence of large values, caused in particular by the periodic noise.

The values of f_0, f_1, and f_2 in Steps 2 and 3 are fixed as follows. We set $f_2 = 8/L$. This means that the sought noise frequency must be above $8/L$ cycles per pixel, i.e. 8 observed cycles inside the patch shaped by the Hann window. The range in which the power law distribution of the spectrum coefficients should be satisfied is set to $f_0 = f_2/4$ (as only a few low frequencies are available) and $f_1 = 0.2$. Usual values for f_2 ensure that $f_1 > f_0$ is satisfied. In previous works [19, 26], the upper limit is set to 0.35 cycle per pixel. The reason behind this is that high frequencies are mostly affected by white noise (cf. Sec. 2.2) and aliasing. In our patch-based

average spectrum, we observed that the 0.35 value is rather optimistic in some experiments. This is probably explained by the particular nature of the considered images, and by the patch-based average spectrum, where high frequencies are penalized (they indeed are likely to correspond to localized phenomena), causing a fall-off with respect to the expected power law.

In Step 4, bilinear interpolation is used to expand the outlier map. The notch filter is obtained after convolving the outlier map M_o (after interpolation) by an isotropic Gaussian kernel of standard deviation 2 pixels, in order to limit ringing artifacts due to strong cutoffs in high frequencies.

The only remaining free parameter is the size L of the patches. Typically, periodic noise in an image with a width of around $500 - 1000$ pixels is satisfactorily removed with L around 100 pixels. The discussion concerning Step 1 should be borne in mind when setting the value of L.

Remark. The boundary effects in the discrete Fourier transform (DFT) motivate us to multiply the patches by a window decreasing to 0 at its boundaries. The discrete cosine transform (DCT) does not suffer from this drawback, since it is equivalent to computing the DFT of an even extension of the initial image along both the x- and y-axes. However, the drawback is to mix information from symmetric directions. We have observed that the proposed algorithm performs equally well with DCT instead of DFT, without the need to multiply the patches with a decreasing window, although the fitting of the power spectrum with the power law is slightly altered. In this report, we use the DFT-based version.

3.3 Illustrative example

Fig. 1 a. shows a 600×581 image i obtained by the Mariner 4 probe. It is impaired by quasi-periodic noise. Since this high frequency noise may be smoothed out in the printed version of the report, the reader is kindly asked to zoom in in the pdf file. The power spectrum is shown in Fig. 1 b. It can be noted that the Fourier coefficients actually tend to decrease with f (the corners are darker than the middle), but the spikes corresponding to the noise periodic pattern can hardly be identified. The horizontal / vertical grid pattern is due to the regular marking on the sides of i. This illustrates the difficulty in automating the notch filter design from the power spectrum alone. It appears that the contribution of the periodic noise is hidden behind the contribution of contours or localized textures. This is confirmed by the distribution of the power spectrum coefficients against the frequency, which shows a decreasing trend with largely scattered points (cf. Fig. 1 c). Fig. 1 d. shows the average power spectrum obtained by averaging the power spectrum of a set of 870 $L \times L = 128 \times 128$ image patches (see (11)) regularly distributed over the whole image at $L/8 = 16$ pixels apart in the $x-$ and $y-$directions. The power law is fitted to this average power spectrum through robust linear regression (we find $A = 11.27$ and $\alpha = 1.47$), see Fig. 1 e. Here, the red line corresponds to the linear trend (between f_0 and f_1 cycle per pixel), and the upper green line corresponds to the 3σ upper limit (beyond f_2). Outliers are above this latter straight line. Note that a few outliers are missed. We can see that a uniform threshold (i.e., constant over the frequency range) would not detect the spikes and would retain most of the low- to middle-frequency components. We also observe a fall-off in the higher frequencies.

The residuals between the average power spectrum and the expected linear relation are normalized as in the left-hand member of (10), giving the so-called *normalized spectrum*, depicted in Fig. 2 a. In this latter image, the spikes are well detached, and easier to detect. We can also see that the power law actually depends on the orientation; though sufficient for our purpose, an isotropic modeling of the spectrum fall-off does not fit the actual distribution well. Here, the dependence is probably due to the orientation of the illumination source (from the bottom to the top of the image), which gives a dominant direction for the shadow distribution. Fig. 2 b. shows

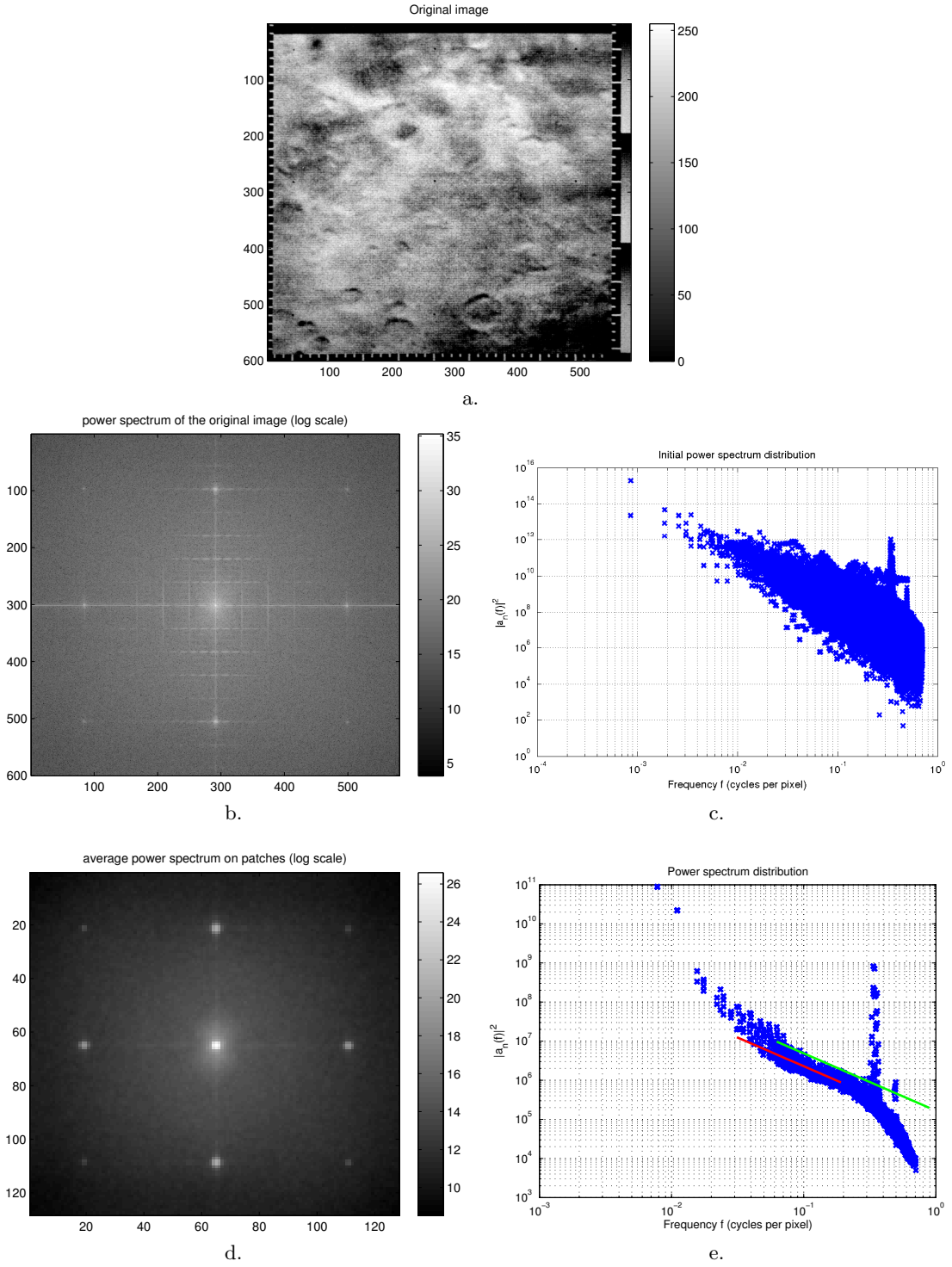

Figure 1: Mariner 4 experiment (1). a: A 600×581 image from the Mariner 4 probe, impaired by pseudo-periodic noise. b: Its power spectrum (log scale). c: Power spectrum distribution against frequency. d: Average power spectrum calculated for a set of 870 128×128 patches from the original image. e: Average power spectrum distribution against frequency (logarithmic scales).

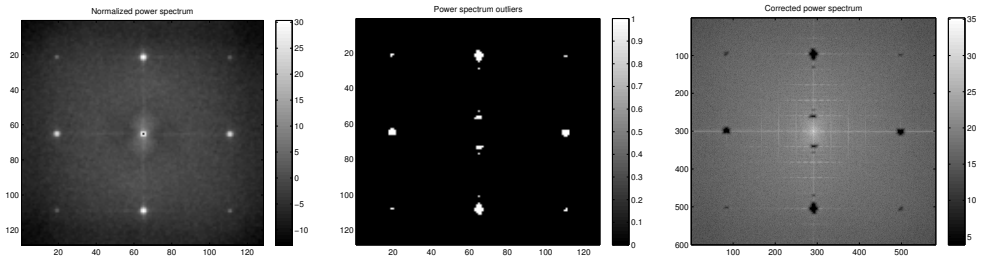

a. b. c.

Figure 2: Mariner 4 experiment (1). a: Normalized average spectrum. b: Outliers. c: Corrected power spectrum.

the outlier localization in the average power spectrum, and the modified spectrum of the original image is shown in Fig. 2 c. (this is the original spectrum multiplied by the notch filter $1 - M_o$, cf. Step 4 in Sec. 3.1). The two peaks in the distribution of the coefficients in Fig. 1 e. correspond respectively to the four spikes at the boundaries of the x- and y-axes, and to the four spikes in the corners. The low-frequency outliers detected on the vertical axis are the few "false positive" points over the green line just above f_2 in Fig. 1 e. The impact of such points is illustrated below.

The output of the proposed algorithm is the de-noised image $\widehat{i}$, and the pseudo-periodic noise component $\widehat{n}$, shown in Fig. 3 a. and b. Following the terminology of Buades et al. [3], the retrieved noise component is called *method noise*. It should ideally consist only of noise; no structure from the original image should be visible in this image. We can see that the periodic noise has been removed from $\widehat{i}$. The pseudo-periodic noise $\widehat{n}$ is much more complicated than a simple sine wave. A close-up view of the original and de-noised images is shown in c. and d. Of course, the white noise component w is not removed by the algorithm.

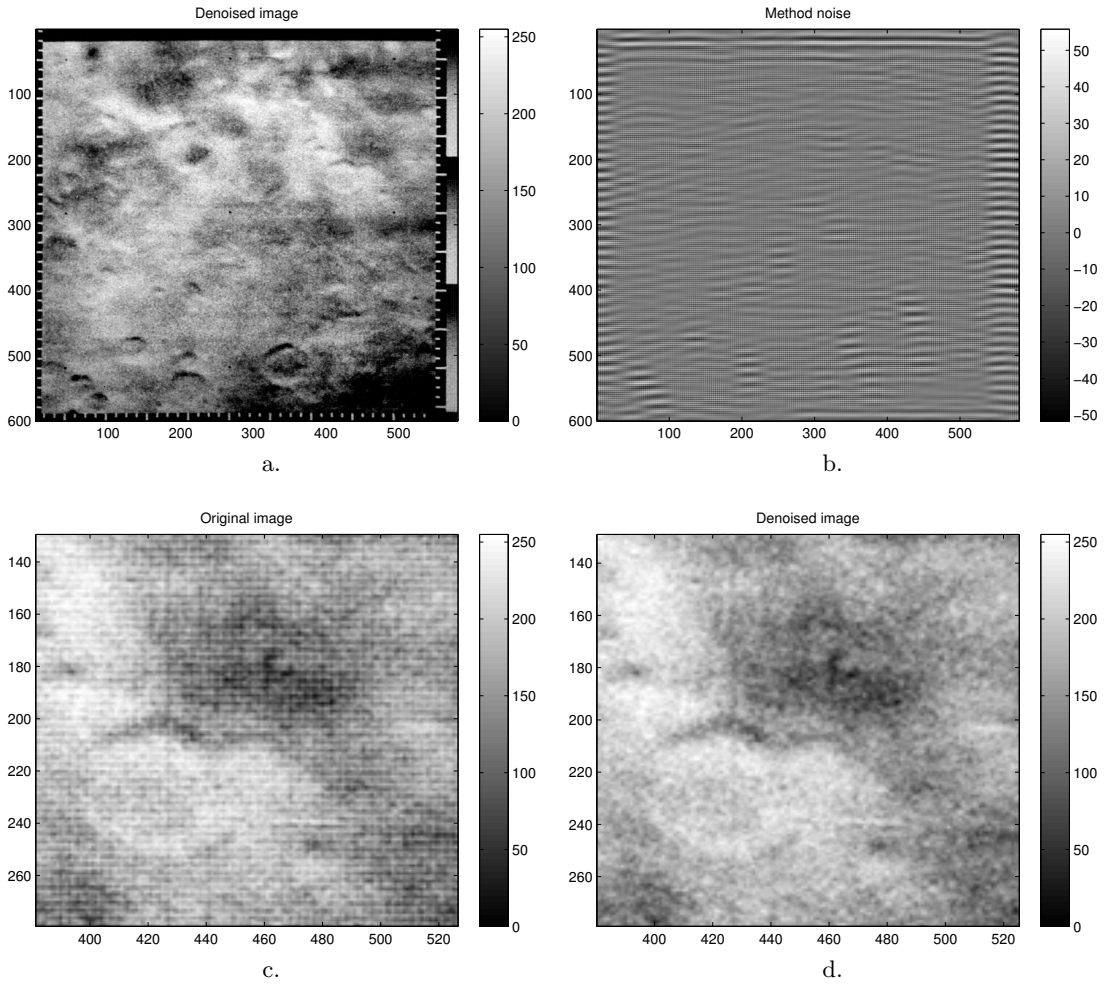

Figure 3: Mariner 4 experiment (1). a: De-Noised image $\widehat{i}$. b: Noise component $\widehat{n}$. c: Close-up view of the noisy image. d: Close-up view of the de-noised image.

4 Experiments

A series of examples is now presented and discussed to illustrate the benefits and limitations of this approach. A synthetic noise is first considered to rely on a reference image when discussing the result of the process (Sec. 4.1). Various noisy images from the literature or the Internet are then processed (Sec. 4.2). A comparison with a blind source separation algorithm is discussed in Sec. 4.3. In the illustrations, the x-component corresponds to the rows and the y-component to the columns.

4.1 Synthetic dataset

Experiments concerning synthetic data are discussed in this section. Synthetic periodic noise is added to a 8-bit noise-free image i_0 of size $X \times Y$. The periodic noise intensity is given by

$$n(x,y) = 50 \sin\left(2\pi \frac{p}{X} x\right) \sin\left(2\pi \frac{q}{Y} y\right) \tag{12}$$

where p and q are parameters governing the frequency of the pseudo-periodic noise along the x- and y-axes, respectively. The unit of n is the gray level. The root mean-square error (RMSE) between the noisy image $i = i_0 + n$ and the ground truth is equal to 25.

In the first experiment, the ground truth image is the standard *Mandrill* image. Here $X = Y = 512$ and we set $L = 128$ (hence $N = 576$ patches, see (11)). In this example, $\alpha = 1.59$ and $A = 11.29$. Fig. 4 and 5 present an example showing noise with a high-frequency y-component and a low-frequency x-component (here $p = 2$ and $q = 200$). The spikes caused by the periodic noise are not visible in the initial spectrum. However, most coefficients are correctly retrieved as upper outliers of the power law distribution. As in the preceding illustrative experiment, the few values just below the 3σ limit do not prevent the de-noising algorithm from giving visually satisfactory results. The reason is that these values correspond to the neighborhood of the detected outliers, which is smoothed out by the Gaussian convolution in Step 4 of the algorithm. Note that the power spectrum distribution shows a constant value for high frequencies. It is probably the effect of the fur which plays the role of strong white noise, in accordance with Sec. 2.2. We can define the RMSE calculated between the retrieved image $\widehat{i}$ and the ground truth (corresponding to the average error on the retrieved intensity of a pixel). Here, the RMSE is equal to 0.598, which is below the intensity quantization level (equal to one gray-level) and far below the original error, which was 25.

We also illustrate the performance of the algorithm with respect to the noise component frequency. The frequency p (respectively q, in cycles per image) spans $[0, X/2]$ (respectively $[0, Y/2]$) in steps of 20 (hence 13×13 tested frequencies), except for values where $\sqrt{(p/X)^2 + (q/Y)^2} < f_2$, since frequencies which are too low are not considered as periodic noise components and are not eliminated by the algorithm. The RMSE is computed for each of these 13×13 frequency pairs. Fig. 6 gives the RMSE map for the 13×13 frequencies (p in ordinate, q in abscissa). The top-left corner corresponds to the skipped low frequencies, and the bottom-right corner to the highest frequencies. We can see that, except for quite low frequencies, the RMSE is below 1, and that in any cases it is much lower than the original error of 25.

In the second experiment, the ground truth image is the standard *Boat* image. As in the previous experiment, $K = 512$ and $L = 128$. Here, $p = 40$ and $q = 100$. In this example, $\alpha = 2.52$ and $A = 8.73$. Fig. 7 and 8 depict an example deliberately chosen for didactic purposes such that the noise components are correlated with the image components. Therefore, the notch filter also removes noise-free image parts. We can see in the close-up view that ringing artifacts appear along the masts parallel to the noise pattern. Such a situation is unavoidable in any notch filter-based approach. Reconstructing the missing coefficients by spectrum interpolation

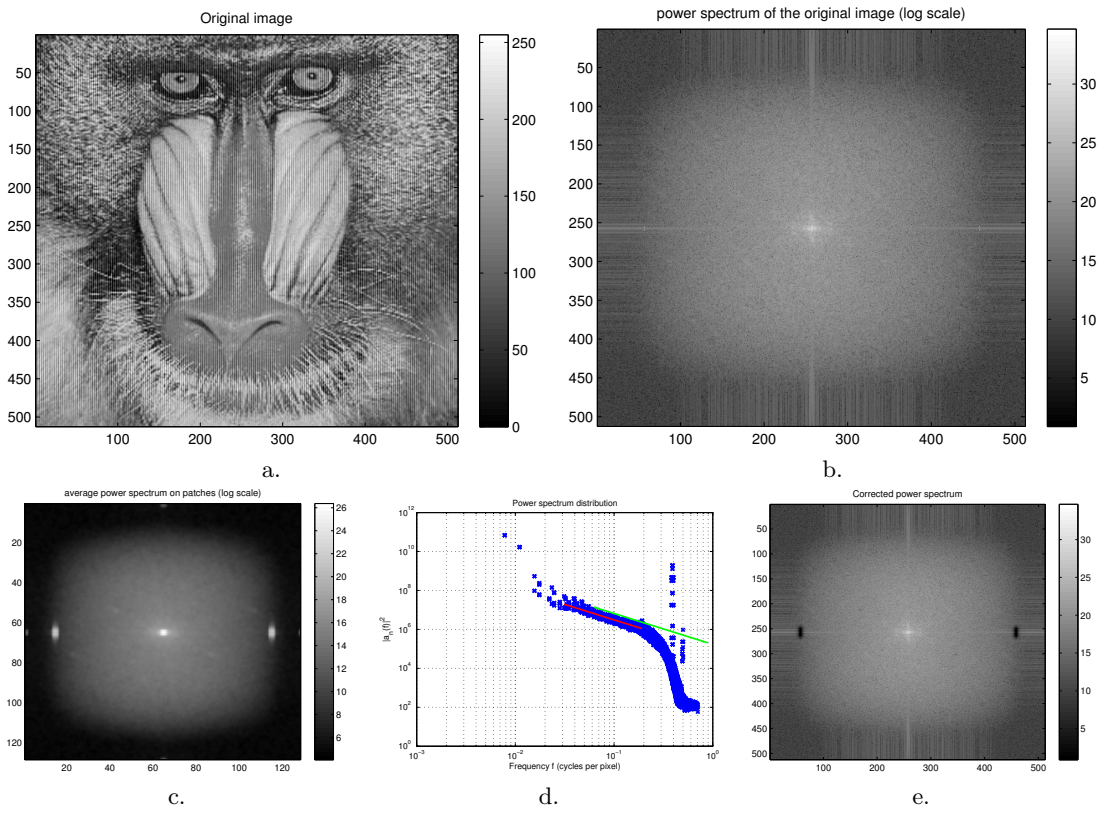

Figure 4: Mandrill experiment. a: Noisy image. b: Power spectrum. c: Average power spectrum. d: Average power spectrum coefficient distribution. e: Corrected power spectrum.

(i.e., spectrum "inpainting") would be required. To the best of our knowledge, this is still an open problem (see the recent PhD thesis [16], and the experiments in [13]). Here, the RMSE is equal to 1.801, which is about three times the RMSE obtained in the preceding example. Fig. 9 gives the error map as above. We can see that the RMSE is slightly larger than in the previous example, precisely because of the correlation between the periodic noise and certain image patterns.

However, we did not observe such a situation in the experiments presented in the following section. It appears that in real images the noise spectrum is mostly well separated from the image spectrum.

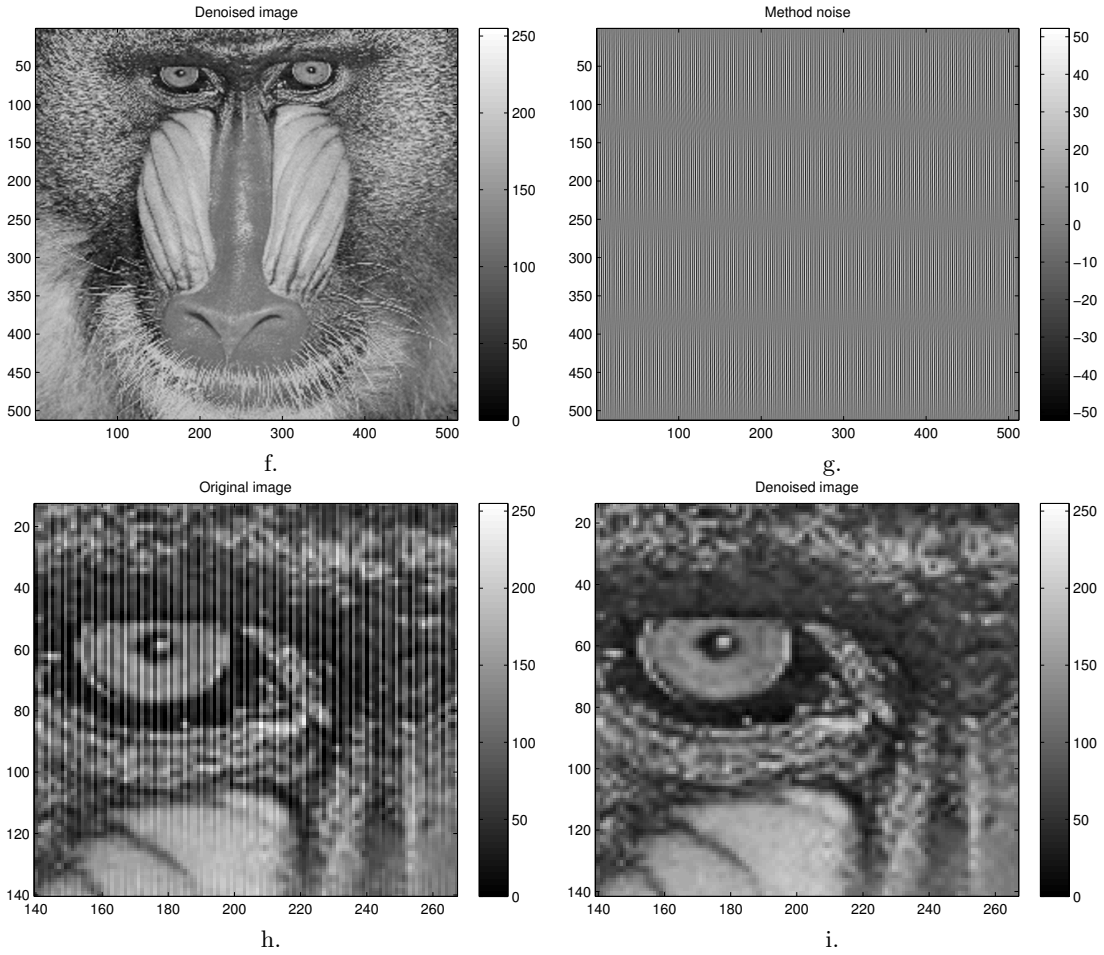

f. g.

h. i.

Figure 5: Mandrill experiment. f: De-Noised image. g: Estimation of the noise. h: Close-up view of the noisy image. i: Close-up view of the de-noised image.

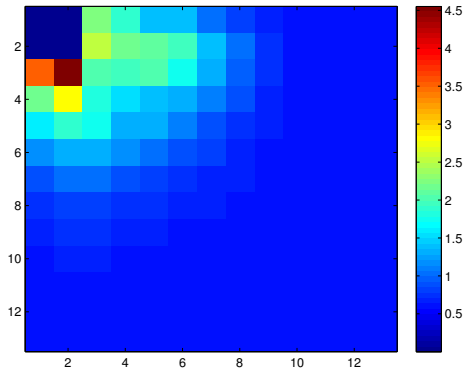

Figure 6: Mandrill experiment. Map of the RMSE as a function of periodic noise frequencies.

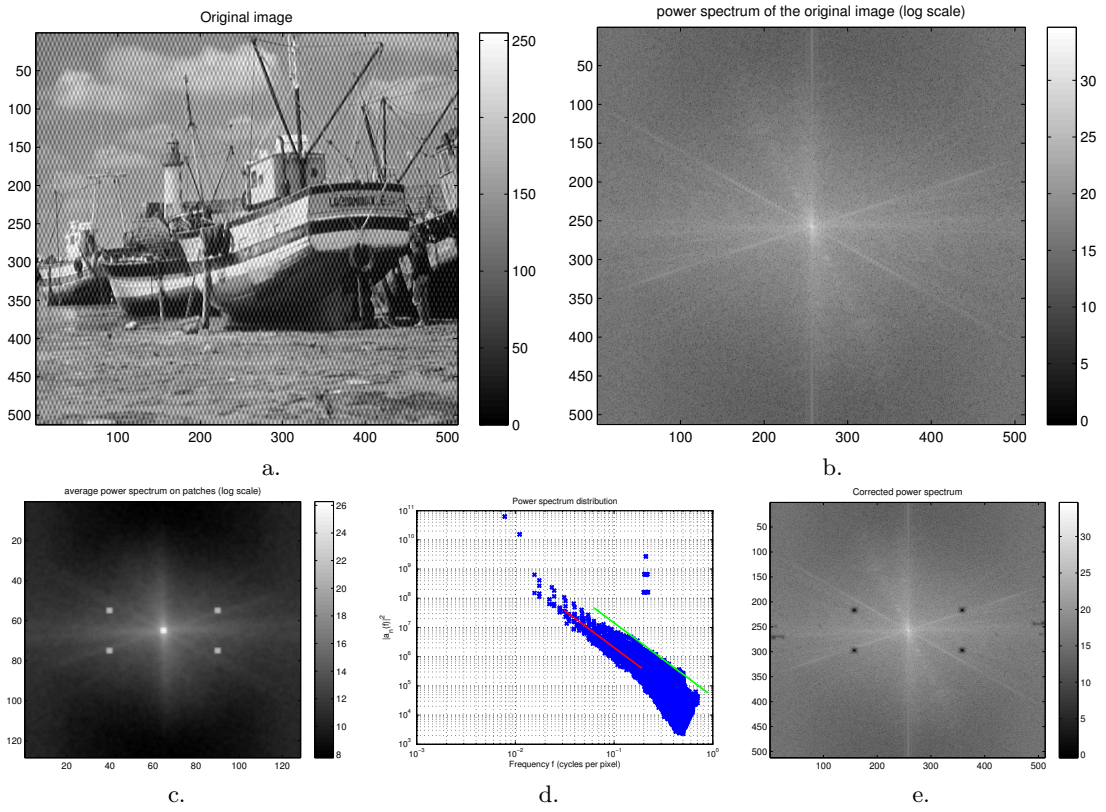

Figure 7: Boat experiment. a: Noisy image. b: Power spectrum. c: Average power spectrum. d: Average power spectrum coefficient distribution. e: Corrected power spectrum.

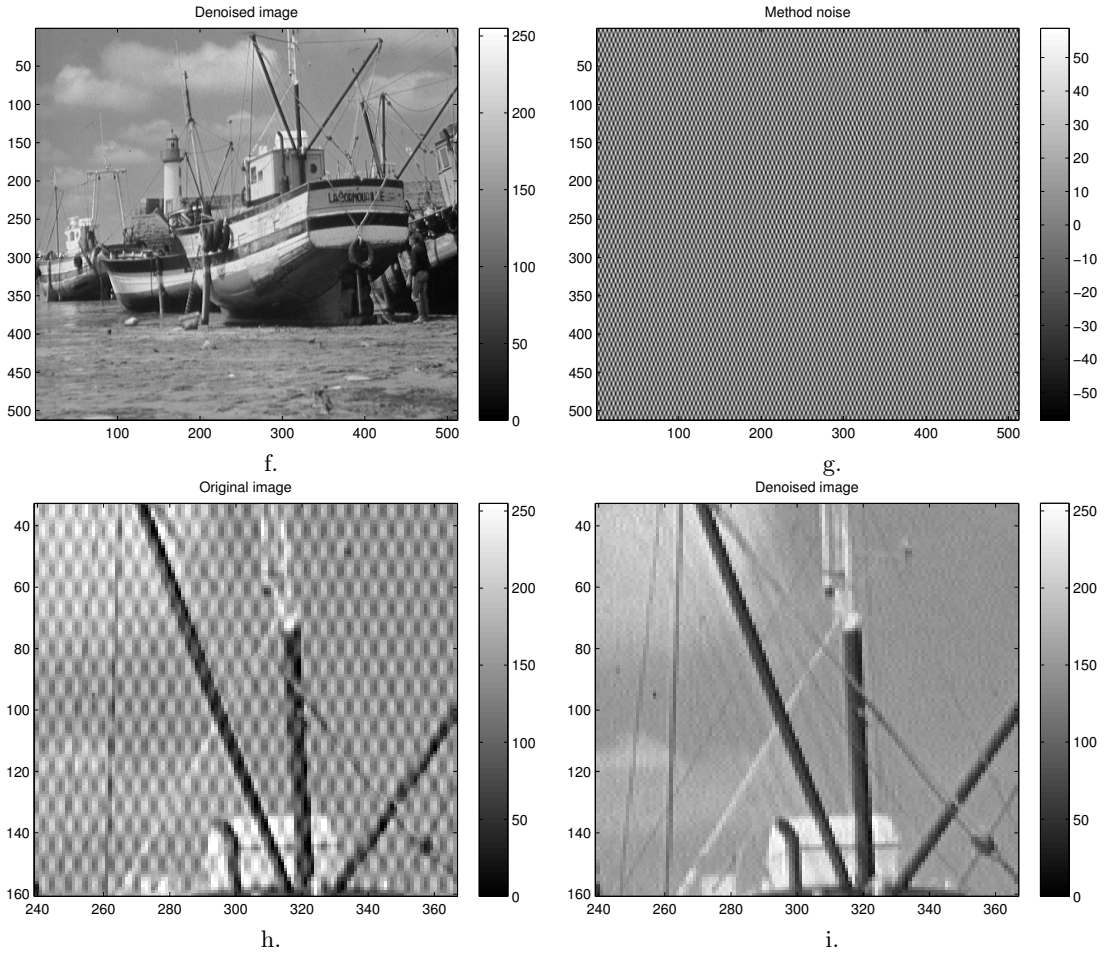

f. g.

h. i.

Figure 8: Boat experiment. f: De-Noised image. g: Estimation of the noise. h: Close-up view of the noisy image. i: Close-up view of the de-noised image.

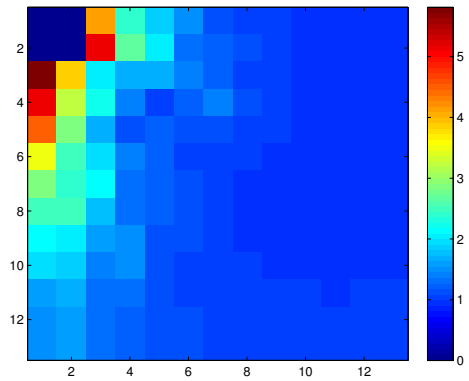

Figure 9: Boat experiment. Map of the RMSE as a function of periodic noise frequencies.

No.	image	size	A	α	L	N	time
1	Mariner4 (Fig. 1-3)	600×581	11.27	1.47	128	870	0.4
2	Apollo (Fig. 10-11)	474×630	10.86	1.38	128	704	0.4
3	Florida (Fig. 12-13)	808×754	11.46	1.91	256	288	0.5
4	Mariner6 (Fig. 14-15)	461×471	9.60	2.31	128	462	0.2
5	Newspaper (Fig. 16-17)	831×730	12.41	1.25	200	572	0.6
6	Bending (Fig. 18-19)	1832×2382	7.36	2.88	300	2255	4.2
7	Mariner6b (fig. 20-21)	483×640	10.14	1.79	128	736	0.4
8	Vicking (fig. 22-23)	1051×1158	7.91	1.81	128	3770	1.6
9a	Halftone (fig. 24-25)	875×1259	12.20	1.20	128	3337	1.5
9b	Halftone (fig. 26-27)	875×1259	6.72	3.08	128	3337	1.5
10a	Halftone-eye (fig. 28-29)	914×1264	12.11	0.98	128	3550	1.5
10b	Halftone-eye (fig. 30-31)	914×1264	9.15	1.94	128	3550	1.5
11	Scanline (fig. 32-33)	254×355	8.10	2.05	64	888	0.1

Table 1: Real images. From left to right: Experiment number; image name and corresponding figures; size of the image; value of A; value of α; length L of the side of the patches; number N of patches covering the image to calculate the average power spectrum; computation time (in seconds, non-optimized Matlab code on Intel Xeon E3-1240 processor).

4.2 Real dataset

For each experiment, we present the noisy image (a), its power spectrum (b), the distribution of this power spectrum (c), the average power spectrum distribution together with the fitting line (in red) and the 3σ upper limit (in green) (d), the average power spectrum of the patches (e), the corrected power spectrum (f), the de-noised image (g), the estimated noise (h), and a close-up view of the noisy (i) and de-noised images (j).

The values of parameter L and of the deduced number N of patches are given in Table 1, together with the values of A and α estimated on the average power spectrum coefficients. Computation times are also mentioned. We can see that $\alpha \simeq 2$ (as expected for "generic" natural images) in the remote sensing images. Images essentially composed of dots (such as the challenging *Apollo*, *Newspaper*, or *Halftone* images) have noticeably different α. The *Bending* image has a larger α. This image cannot be considered as a natural one, as explained briefly below, which explains its specific α and A values.

The original images were found on the Internet:

- The image for experiment 1 comes from:
  `http://www.exploratorium.edu/mars/earlymissions.php`
- The images for experiments 2 to 5 come from [11]: `www.imageprocessingplace.com/`
- The image for experiment 7 comes from: `petermasek.tripod.com/mariner67.html`
- The image for experiment 8 come from: `http://petermasek.tripod.com/viking.html`
- The images for experiments 9 and 10 come from `nullprogram.com/blog/2011/10/13/`
- The image for experiment 11 comes from `scanlines.hazard-city.de`

Experiment 1 (Fig. 1-3) was fully discussed in Sec. 3.3.

In Experiment 2 (Fig. 10-11), the original image is composed of separate shapes (see close-up views) and is an extreme case of pseudo-periodic noise. The average power spectrum is dominated by the noise component and can only marginally be assimilated to the spectrum of a natural image. This explains the aspect of the power spectrum distribution which is quite widely spread. In spite of this, the automated process enables us to detect the noise component, and to reconstruct the image, with only limited residual noise patterns. The complex noise pattern in the Fourier domain makes it all the more convenient to have an automated process. Note that a seemingly better reconstruction is obtained in [11] by manually picking well-selected spikes.

Experiment 3 (Fig. 12-13) shows strong periodic striping in the sea in this satellite image of Florida. This explains the vertical straight lines in the spectrum. In addition to these lines, "blobs" at the center of the top/bottom and left/right boundaries of the images are also detected as outliers to the spectrum distribution. They are certainly explained by aliasing, another cause of spikes in the power spectrum which was not taken into account in this study. This is confirmed by the sharp, pixelized aspect of the coast in the close-up view. As a consequence, the method noise also contains information about the image edges. As expected, white noise is not discarded by the proposed algorithm and is still noticeable. Let us note that an approach to detecting aliasing based on statistical properties of the spectrum is available in [6].

Experiment 4 (Fig. 14-15) is another example of complex noise appearing in remote sensing imaging, which is successfully removed. High-frequency components can be noted in the corners of the spectrum image.

Experiment 5 (Fig. 16-17) deals with halftone printing used in newspapers. In this technique, gray levels are simulated by dots of various sizes, distributed along a regular grid. It is thus possible to consider the image reconstruction as a pseudo-periodic noise removal problem. Although the linearity of the power spectrum distribution stops before the 0.2 cycle per pixel limit, we are still able to detect the spikes. We can see in the close-up view of the de-noised image that the largest dots are still visible, and that subsequent processing is certainly required to obtain a better reconstruction.

Experiment 6 (Fig. 18-19) deals with data from experimental solid mechanics. This experiment is an application of the proposed algorithm to non-natural images. Fig. 18 a. shows a shear strain map measured on the surface of a reinforced notched beam subjected to three-point bending. It is obtained using the so-called "grid method", which consists of marking the surface with a regular pattern (a grid), taking pictures of this pattern during a test, and extracting the phases and their derivatives from the grid images using the windowed Fourier transform [2]. The displacement and strain maps are indeed respectively proportional to the phase and phase derivative changes between current and reference grid images. Low-frequency parasitic fringes like those shown in this figure sometimes appear on the maps. They are due to various causes, such as manufacturing defects of the grid. In the current case, these fringes are likely due to slight regular defects of the grid which are not correctly compensated for by using the process described in [2]. Of course, this image cannot be considered as a "natural" image. Here, the power spectrum distribution is satisfied up to 0.06 cycle per pixel, instead of the 0.2 value used in the algorithm in Sec. 3.1. "Blobs" can be seen in the de-noised image. They are actually caused by sensor noise which propagates to the strain map [24, 12] as spatially correlated noise. We have shown here an example where the automated process provides satisfactorily results. However, the power law assumption is in general not valid for strain maps. They still need hand-tuned dedicated approaches [13].

In Experiment 7 (fig. 20-21), we can see that the complex noise pattern has been correctly identified, in spite of the large number of spikes to remove.

In Experiment 8 (fig. 22-23), the three pairs of spikes caused by vertical striping have been

correctly identified as outliers in the power spectrum distribution. We can see that the series of dots localized in the middle of the image has not been removed, as its contribution to the average spectrum is not meaningful. The close-up view of the de-noised image shows that the vertical stripes have mainly been smoothed out but are still slightly visible.

Experiment 9a (fig. 24-25) is another example with halftone printing, the effect being more pronounced. The close-up view shows that the dots are replaced by a pattern, which is of course the inverse Fourier transform of the notch filter, as expected in this deconvolution approach. In experiment 9b (fig. 26-27), we restrict the fitting of the power law to the linear part in the logarithmic distribution (i.e., we change the value of f_2 from 0.2 to 0.1). We can see that the resulting corrected spectrum is limited to its center part, resulting in a smoother image. Note that the α parameter is significantly different from 2, although the power law hypothesis is still reasonable.

Experiment 10a and 10b (fig. 28-31) is the same kind of experiment as the previous one, confirming that the power law distribution is a sound assumption, but that the valid range is narrower in this case than in natural images.

Experiment 11 (fig. 32-33) is an experiment dealing with scanline removal. This image is a photograph of an image appearing on a CRT monitor and shows a characteristic black spacing between the lines. Line removing is quite challenging because of the limited resolution of the input image. We can see that the pronounced artifacts due to aliasing visible in the spectrum of the original image are discarded by averaging the patch spectra.

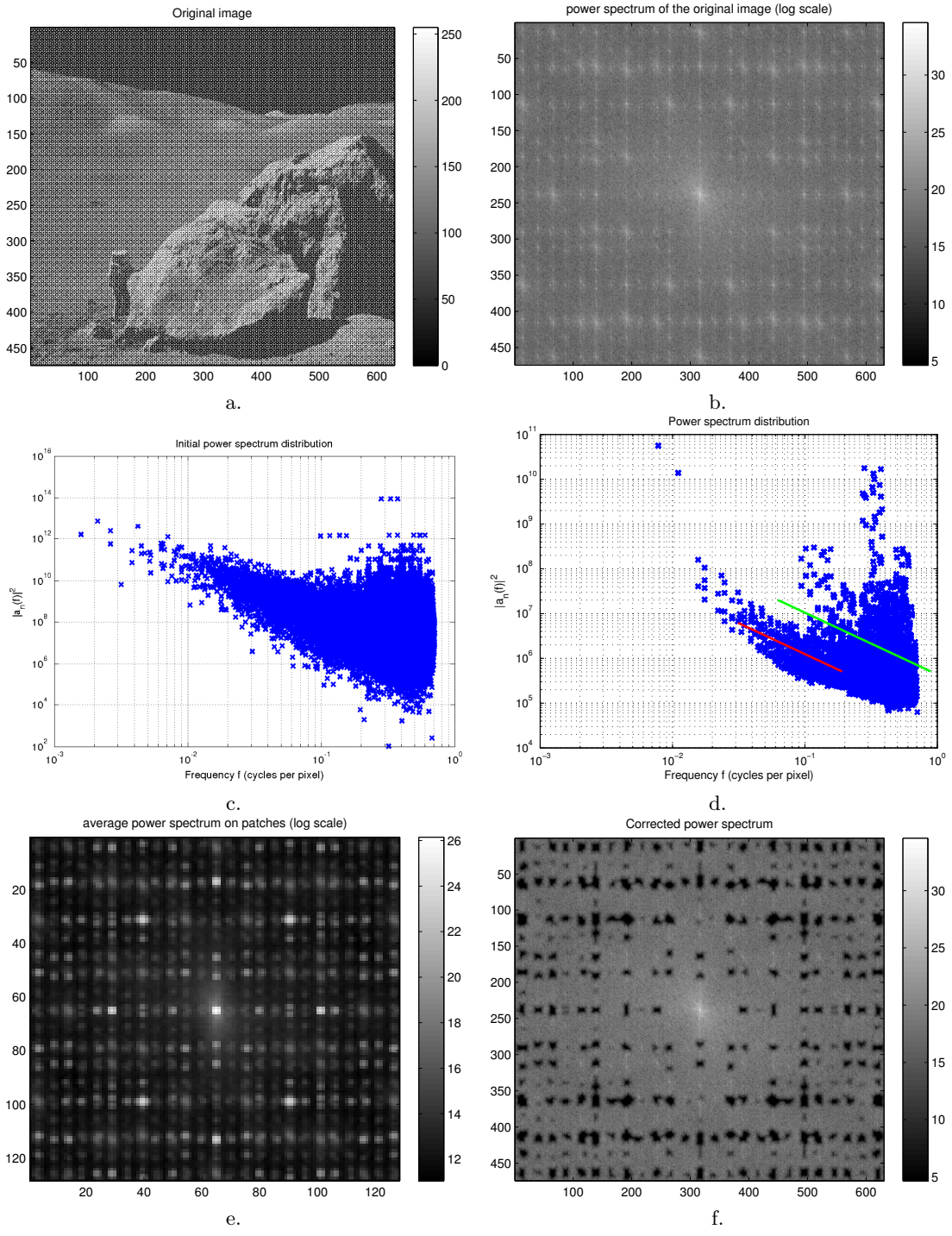

Figure 10: Apollo experiment (2). a: Noisy image. b: Power spectrum. c: Power spectrum coefficient distribution. d: Average power spectrum distribution. e: Average power spectrum. f: Corrected power spectrum.

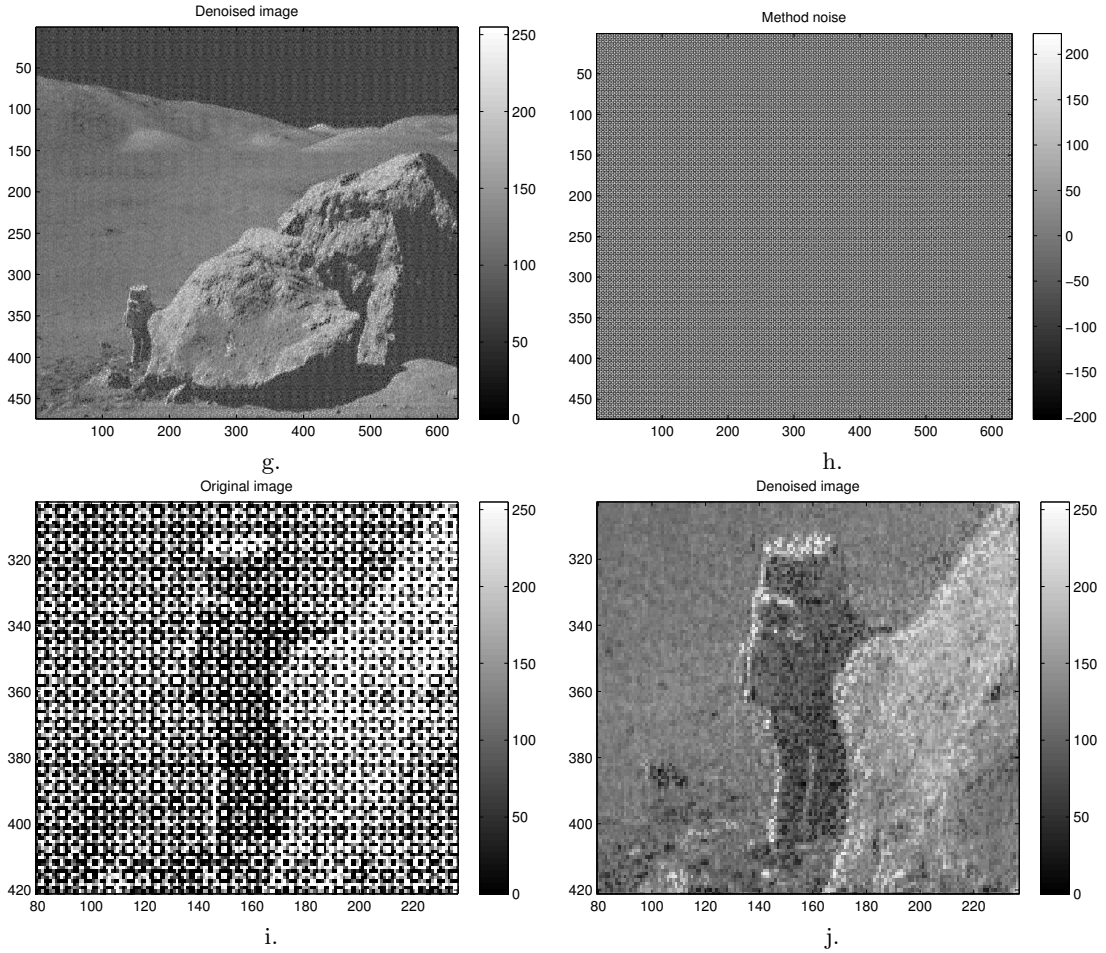

g. h. i. j.

Figure 11: Apollo experiment (2). g: De-Noised image. h: Estimation of the noise. i: Close-up view of the noisy image. j: Close-up view of the de-noised image.

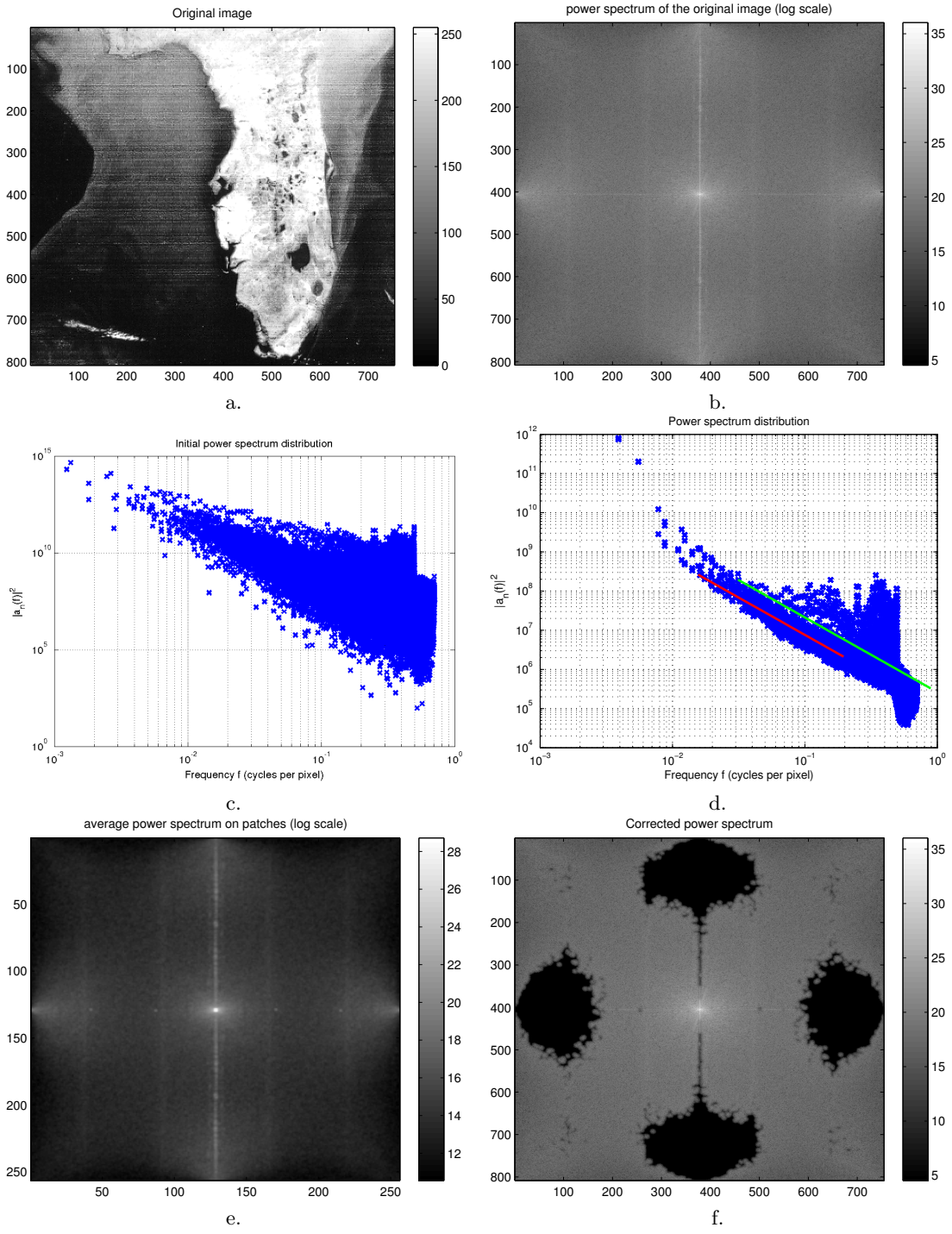

Figure 12: Florida experiment (3). a: Noisy image. b: Power spectrum. c: Power spectrum coefficient distribution. d: Average power spectrum distribution. e: Average power spectrum. f: Corrected power spectrum.

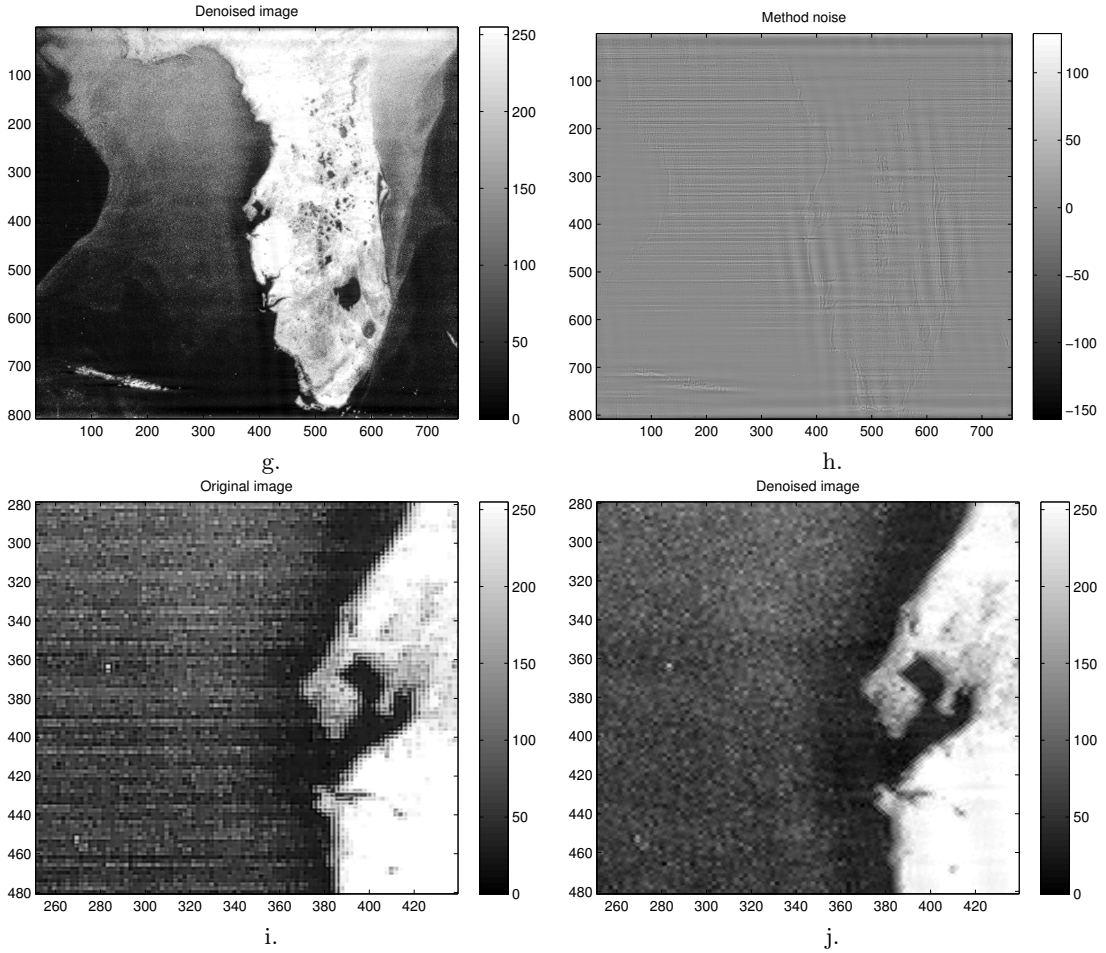

g. h.

i. j.

Figure 13: Florida experiment (3). g: De-Noised image. h: Estimation of the noise. i: Close-up view of the noisy image. j: Close-up view of the de-noised image.

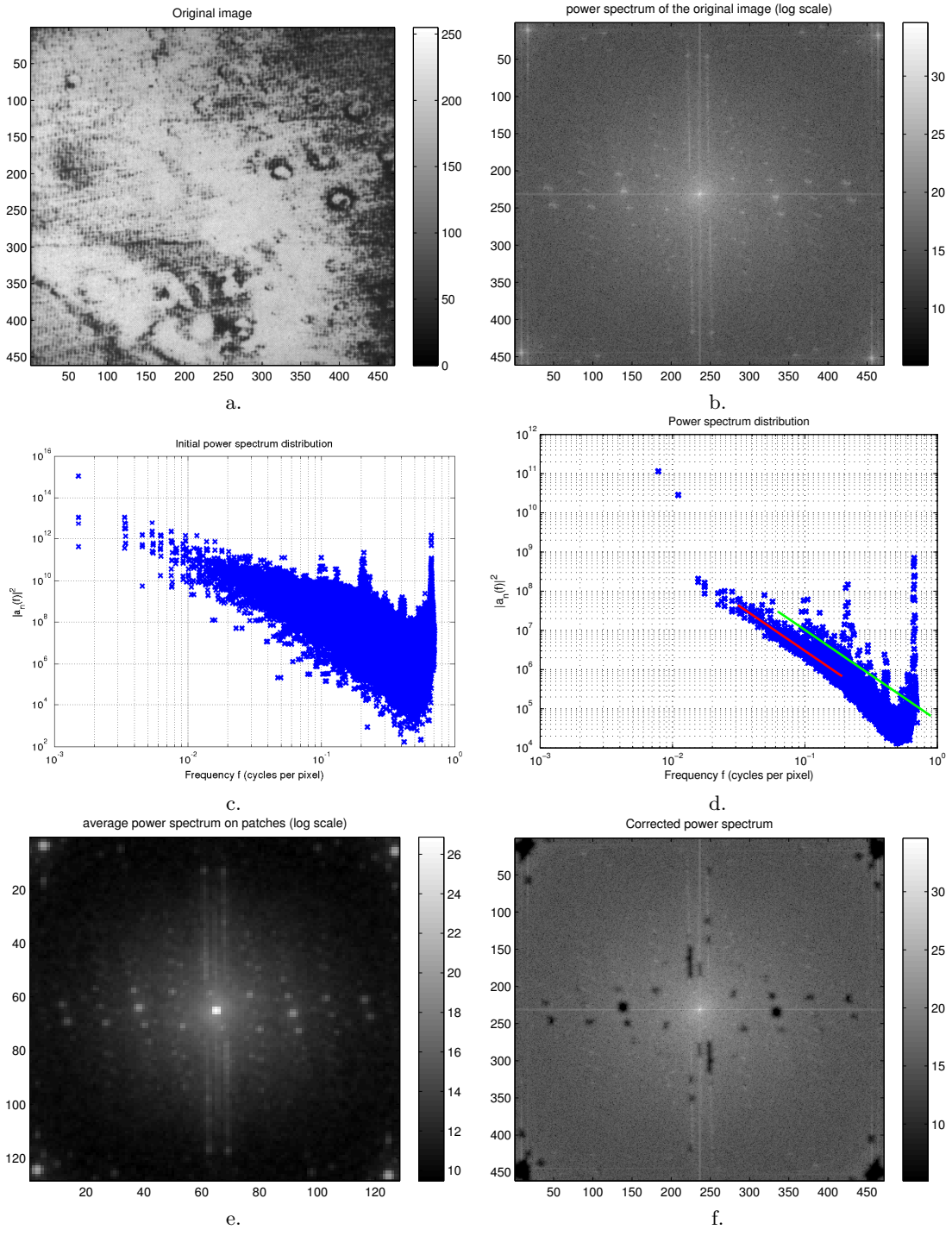

Figure 14: Mariner6 experiment (4). a: Noisy image. b: Power spectrum. c: Power spectrum coefficient distribution. d: Average power spectrum distribution. e: Average power spectrum. f: Corrected power spectrum.

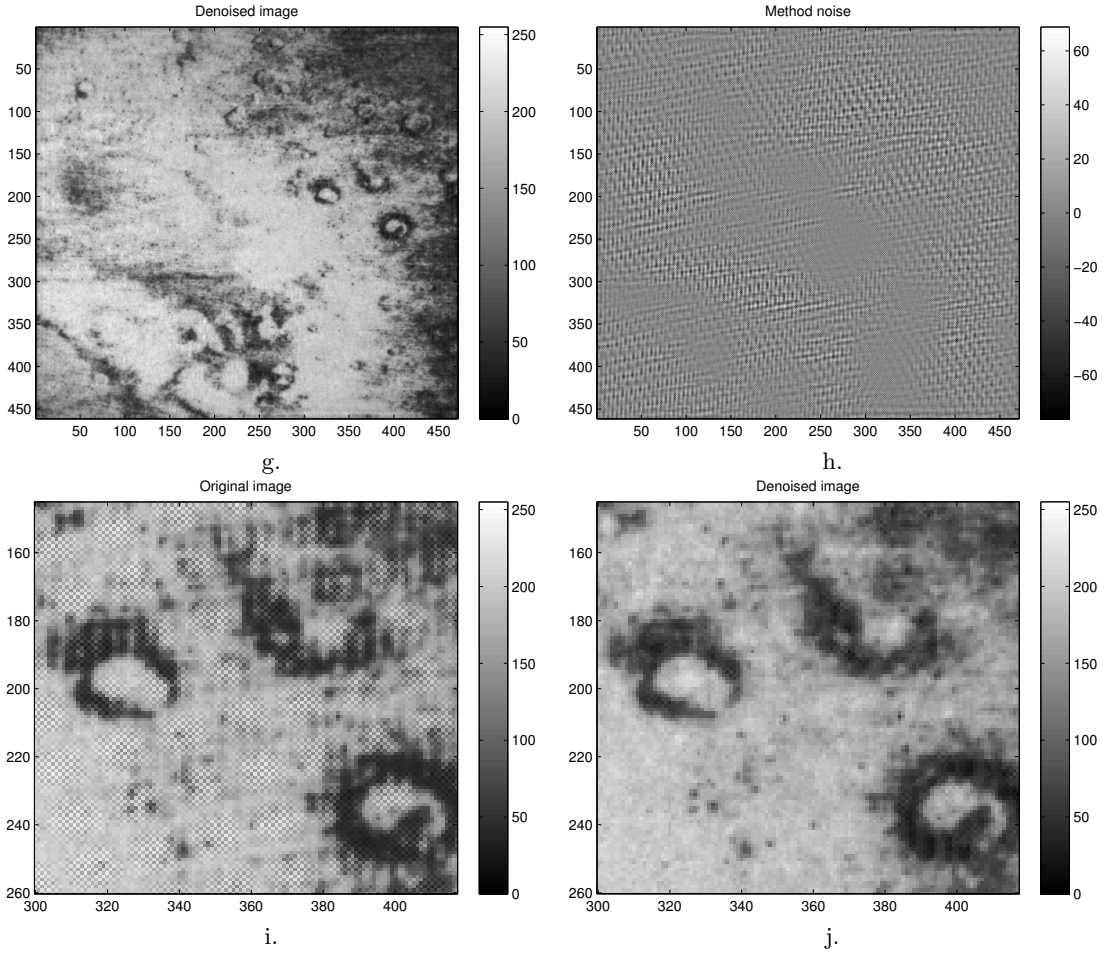

Figure 15: Mariner 6 experiment (4). g: De-Noised image. h: Estimation of the noise. i: Close-up view of the noisy image. j: Close-up view of the de-noised image.

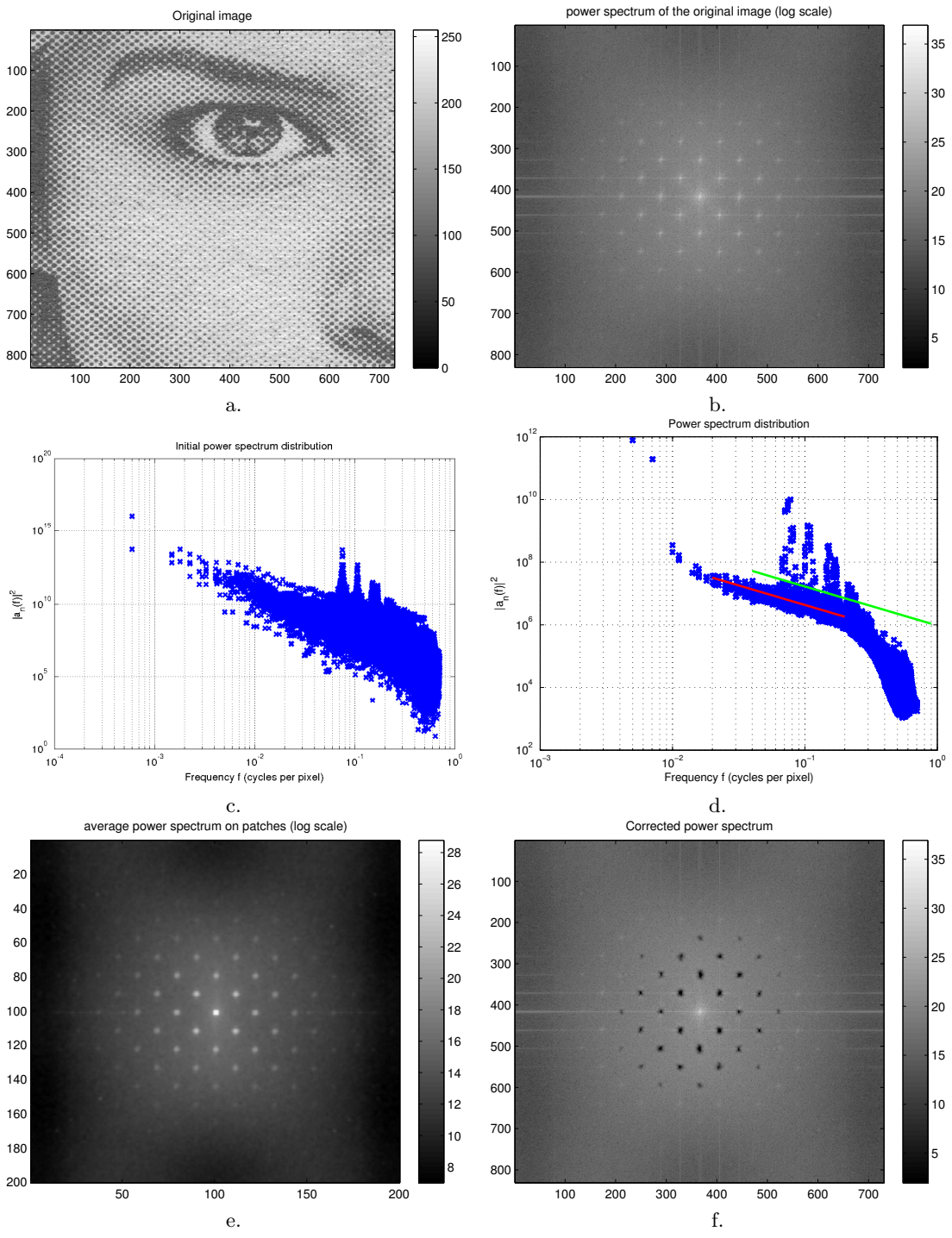

Figure 16: Newspaper experiment (5). a: Noisy image. b: Power spectrum. c: Power spectrum coefficient distribution. d: Average power spectrum distribution. e: Average power spectrum. f: Corrected power spectrum.

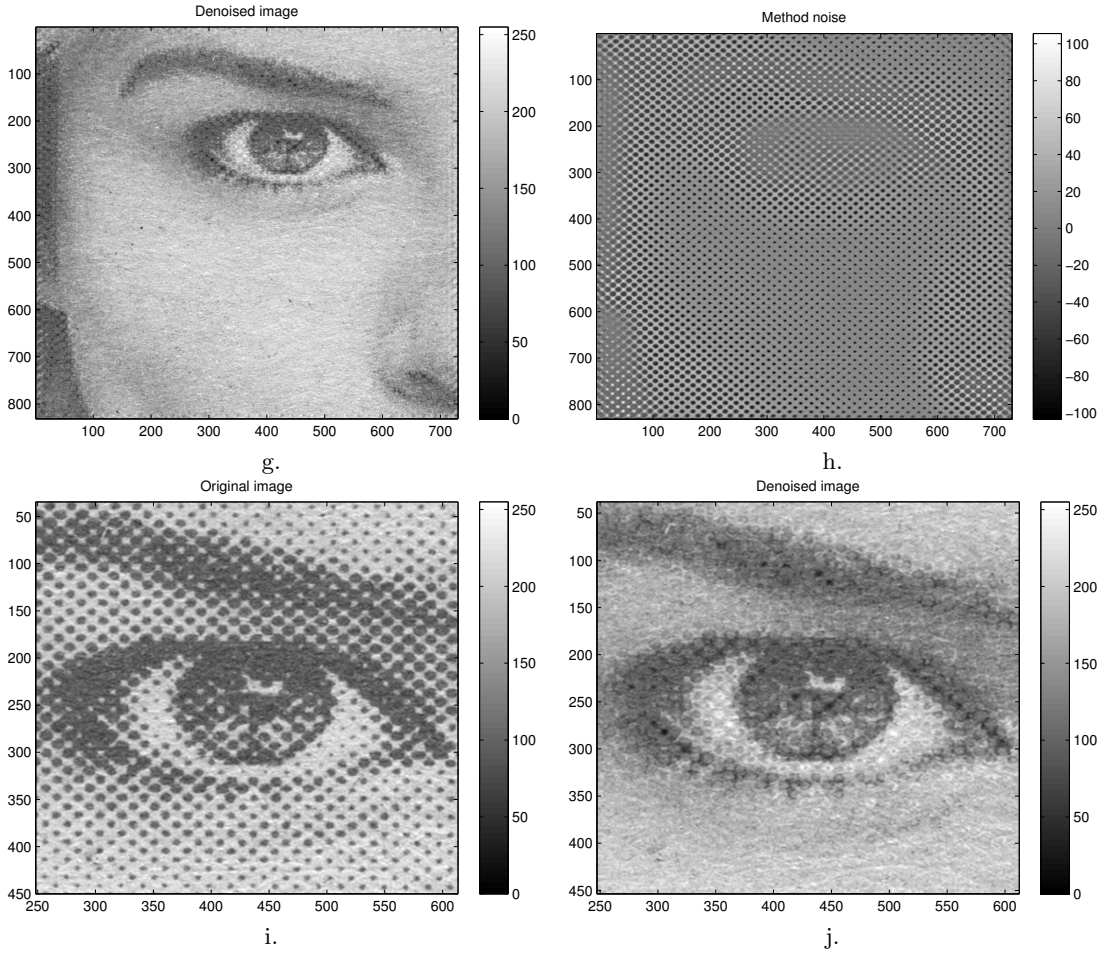

g. h. i. j.

Figure 17: Newspaper experiment (5). g: De-Noised image. h: Estimation of the noise. i: Close-up view of the noisy image. j: Close-up view of the de-noised image.

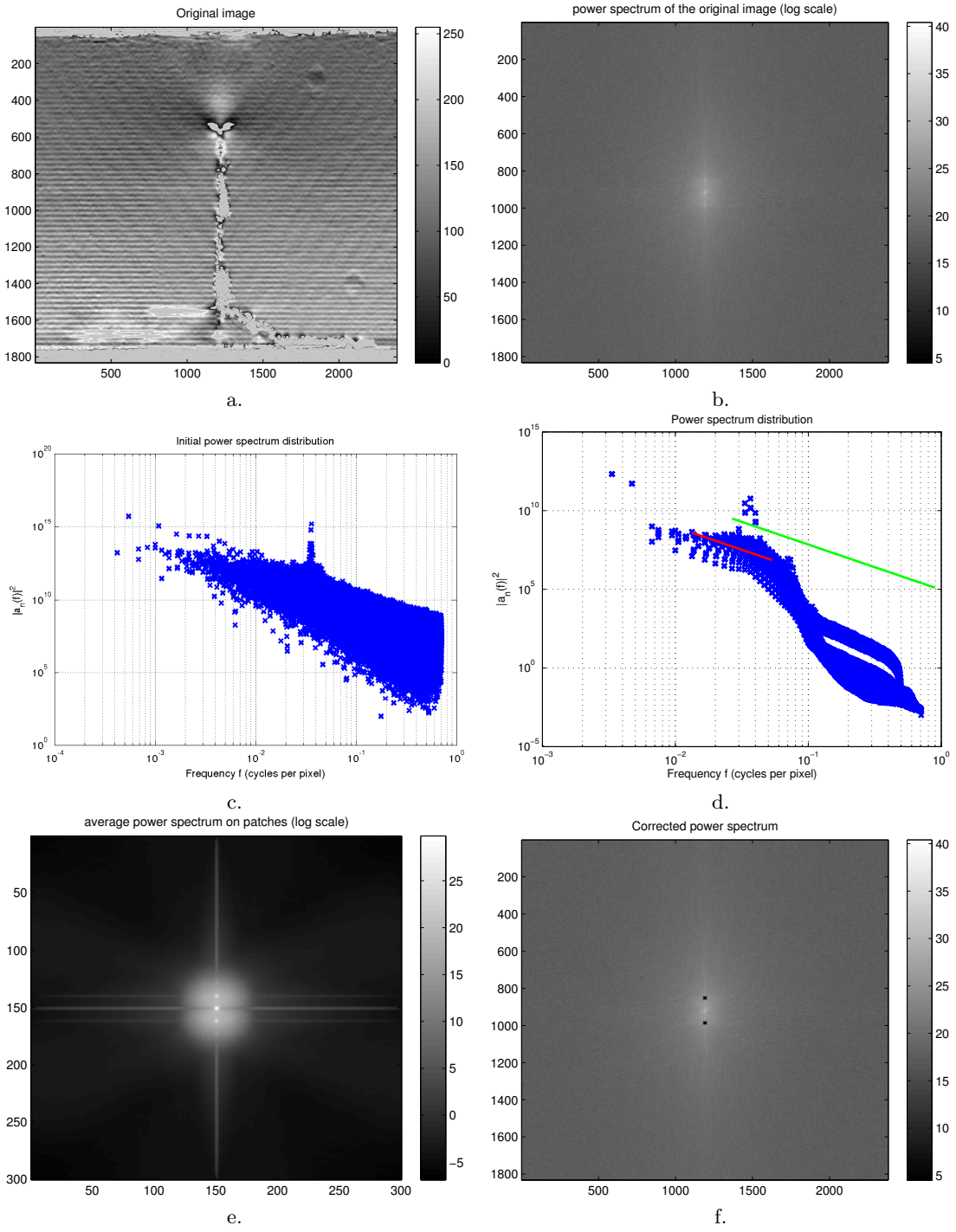

Figure 18: Bending experiment (6). a: Noisy image. b: Power spectrum. c: Power spectrum coefficient distribution. d: Average power spectrum distribution. e: Average power spectrum. f: Corrected power spectrum.

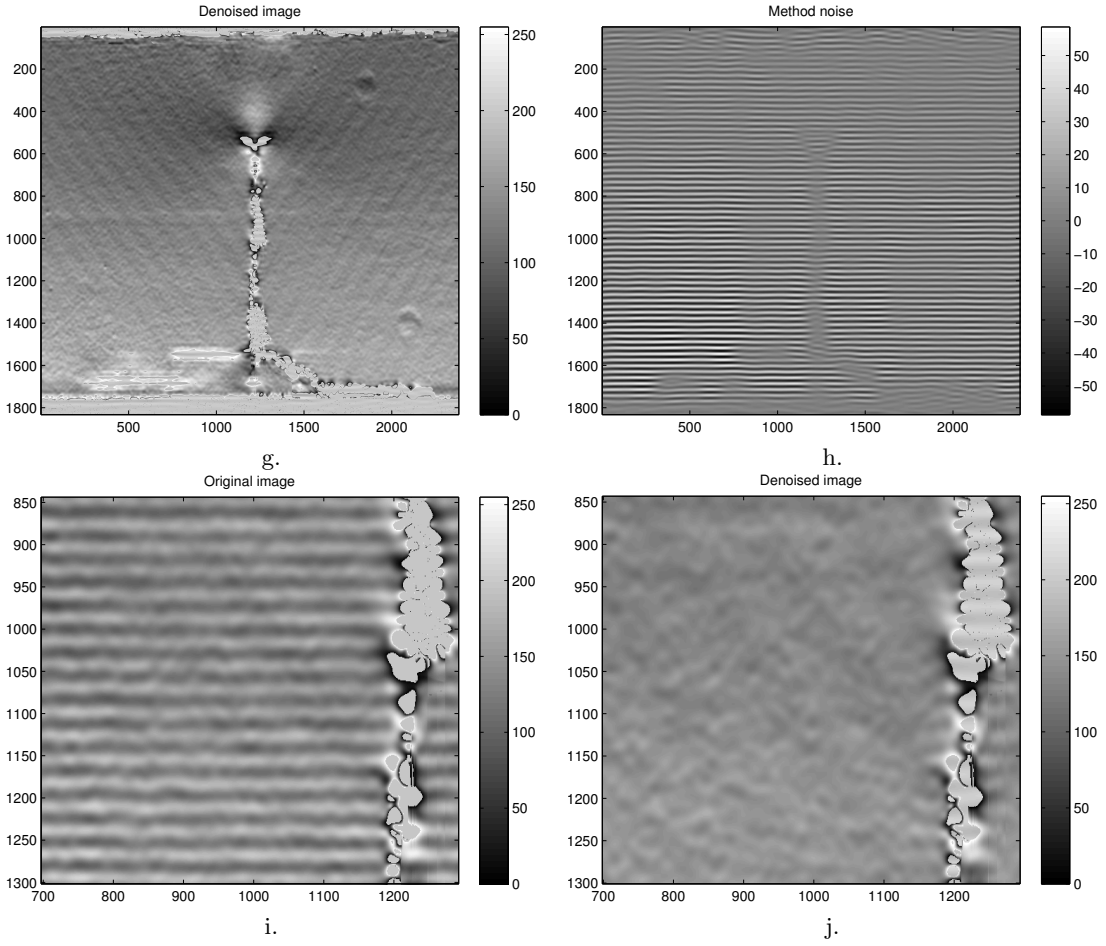

Figure 19: Bending experiment (6). g: De-Noised image. h: Estimation of the noise. i: Close-up view of the noisy image. j: Close-up view of the de-noised image.

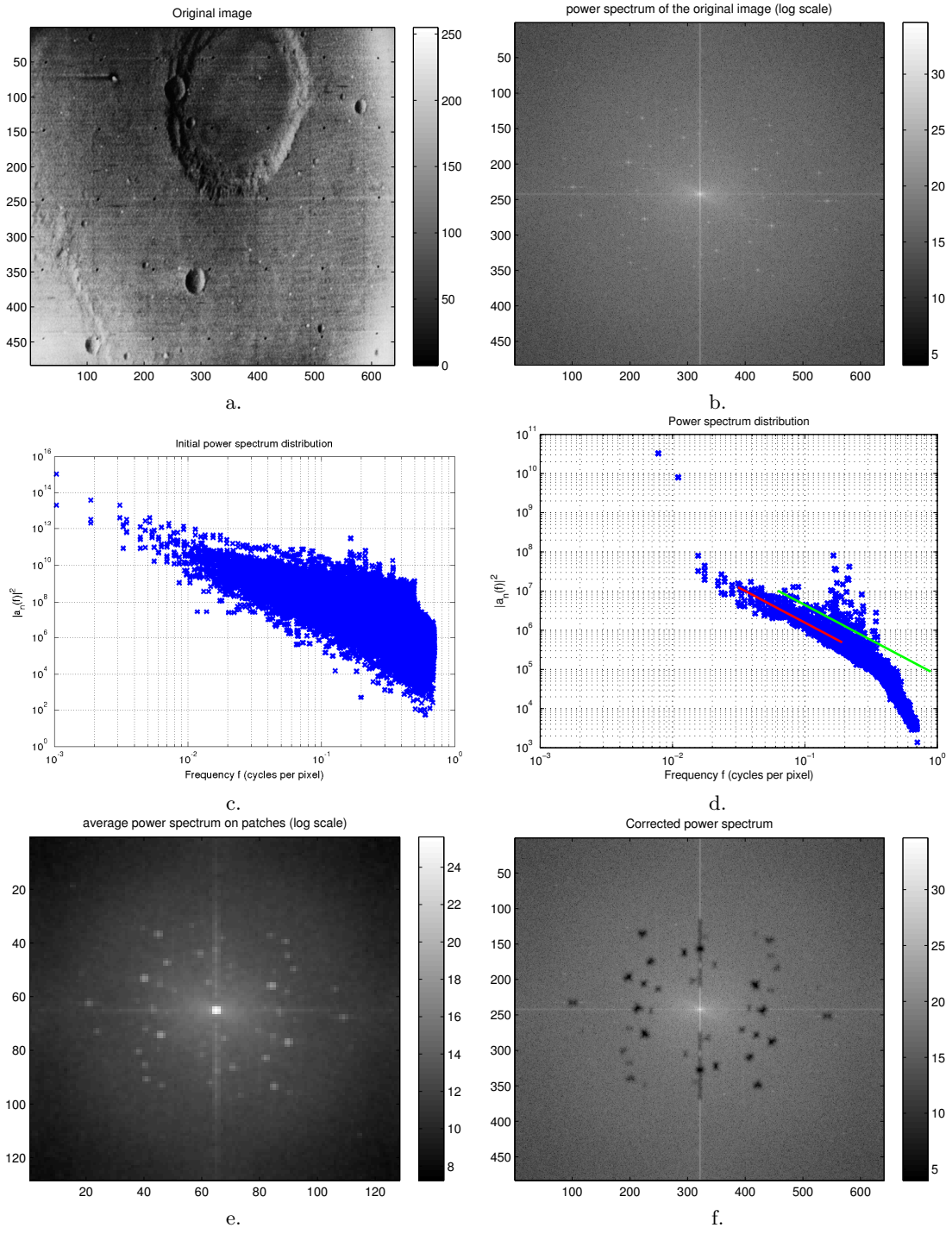

Figure 20: Mariner6b experiment (7). a: Noisy image. b: Power spectrum. c: Power spectrum coefficient distribution. d: Average power spectrum distribution. e: Average power spectrum. f: Corrected power spectrum.

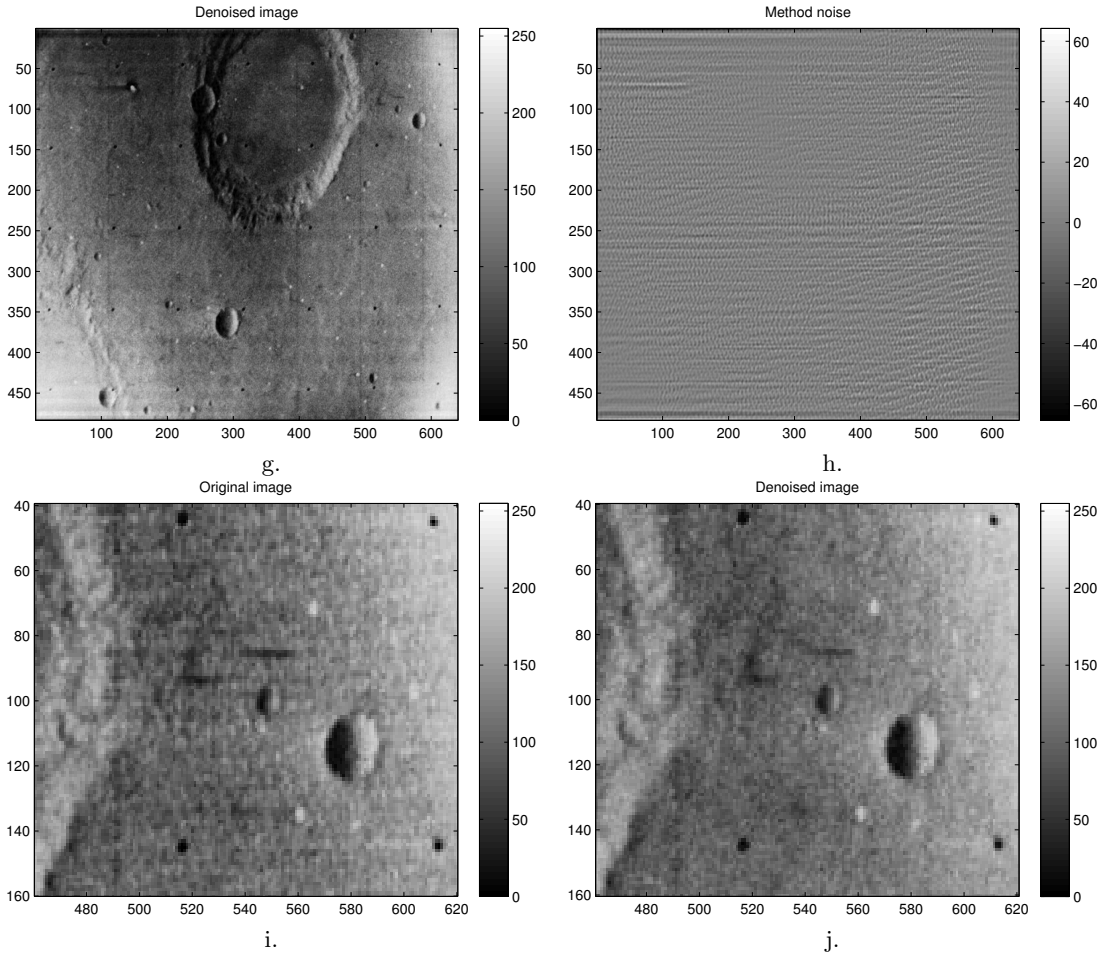

Figure 21: Mariner6b experiment (7). g: De-Noised image. h: Estimation of the noise. i: Close-up view of the noisy image. j: Close-up view of the de-noised image.

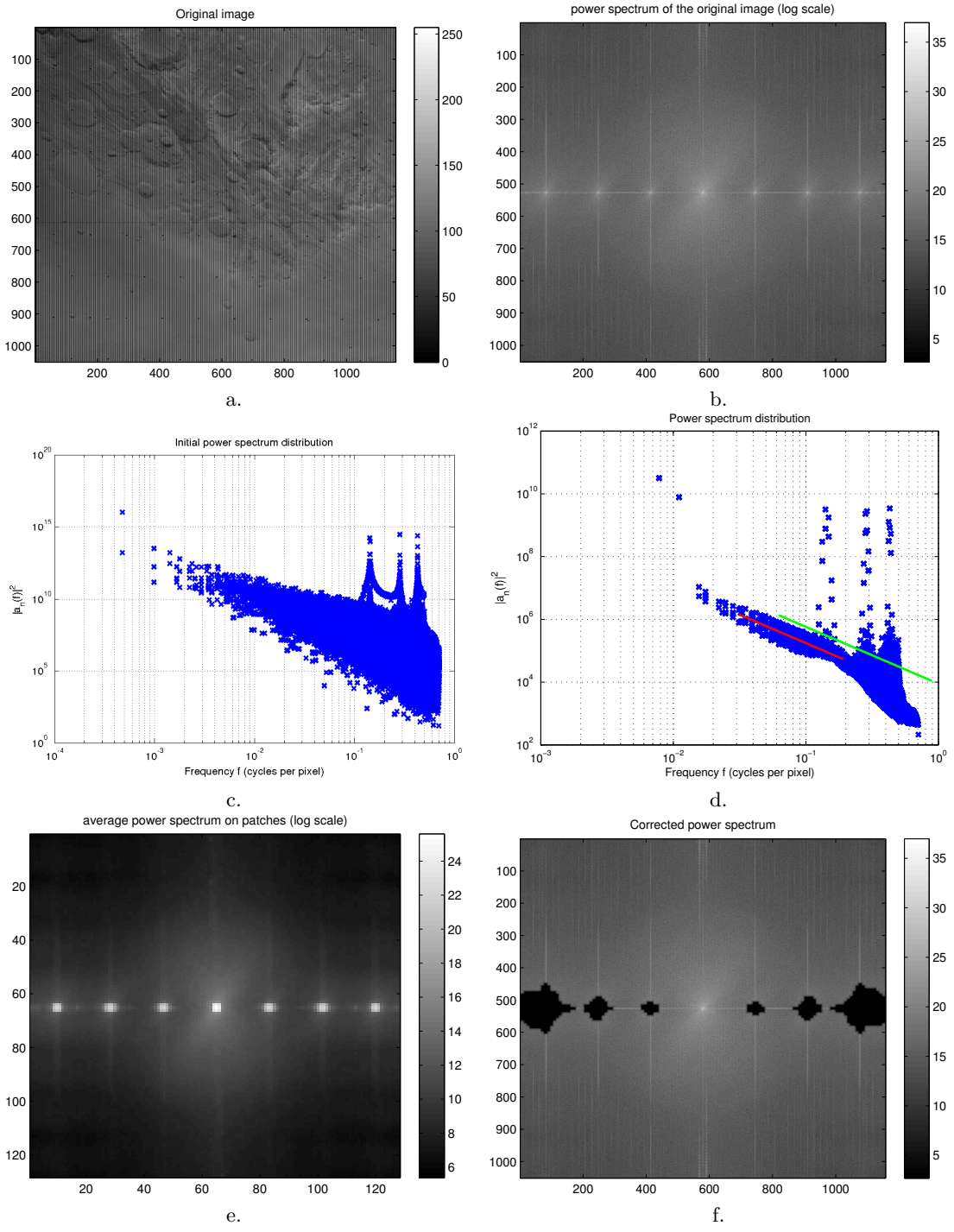

Figure 22: Vicking experiment (8). a: Noisy image. b: Power spectrum. c: Power spectrum coefficient distribution. d: Average power spectrum distribution. e: Average power spectrum. f: Corrected power spectrum.

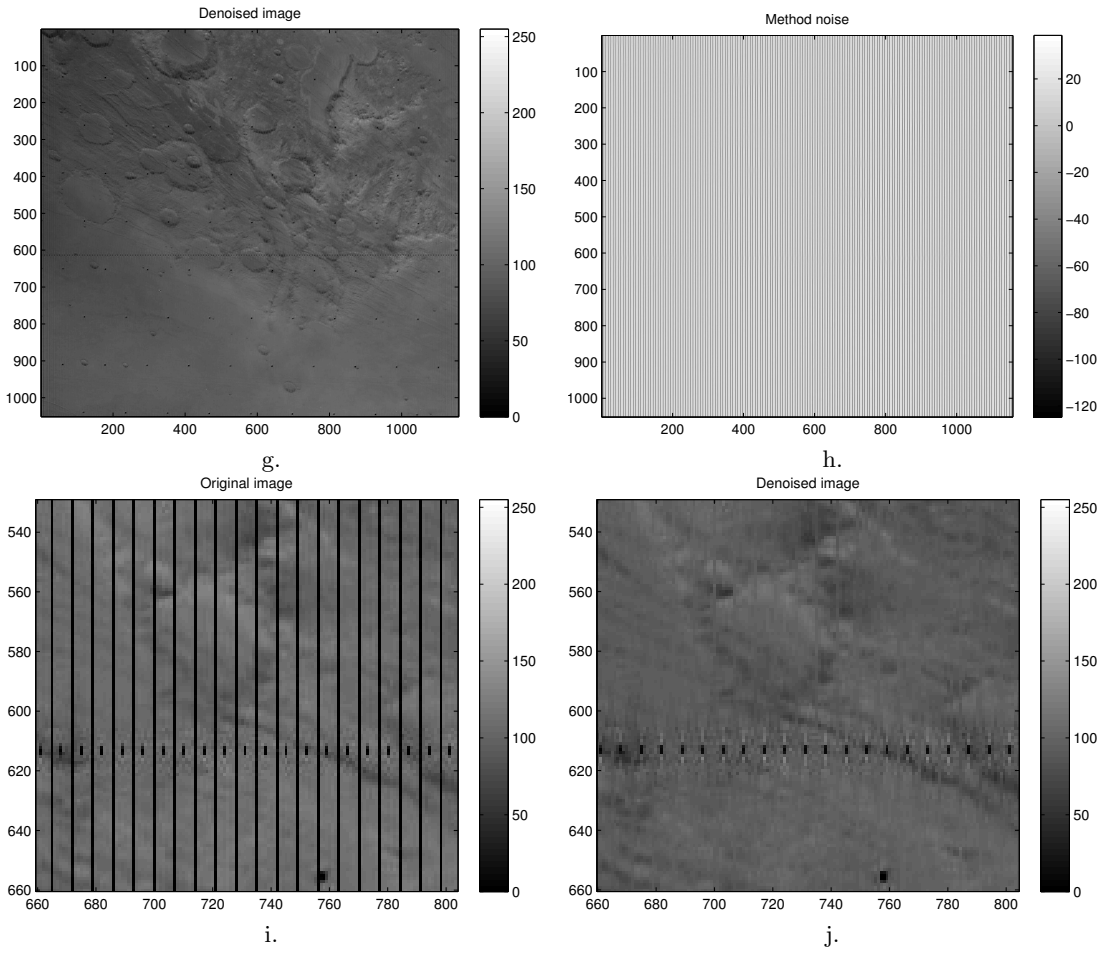

Figure 23: Vicking experiment (8). g: De-Noised image. h: Estimation of the noise. i: Close-up view of the noisy image. j: Close-up view of the de-noised image.

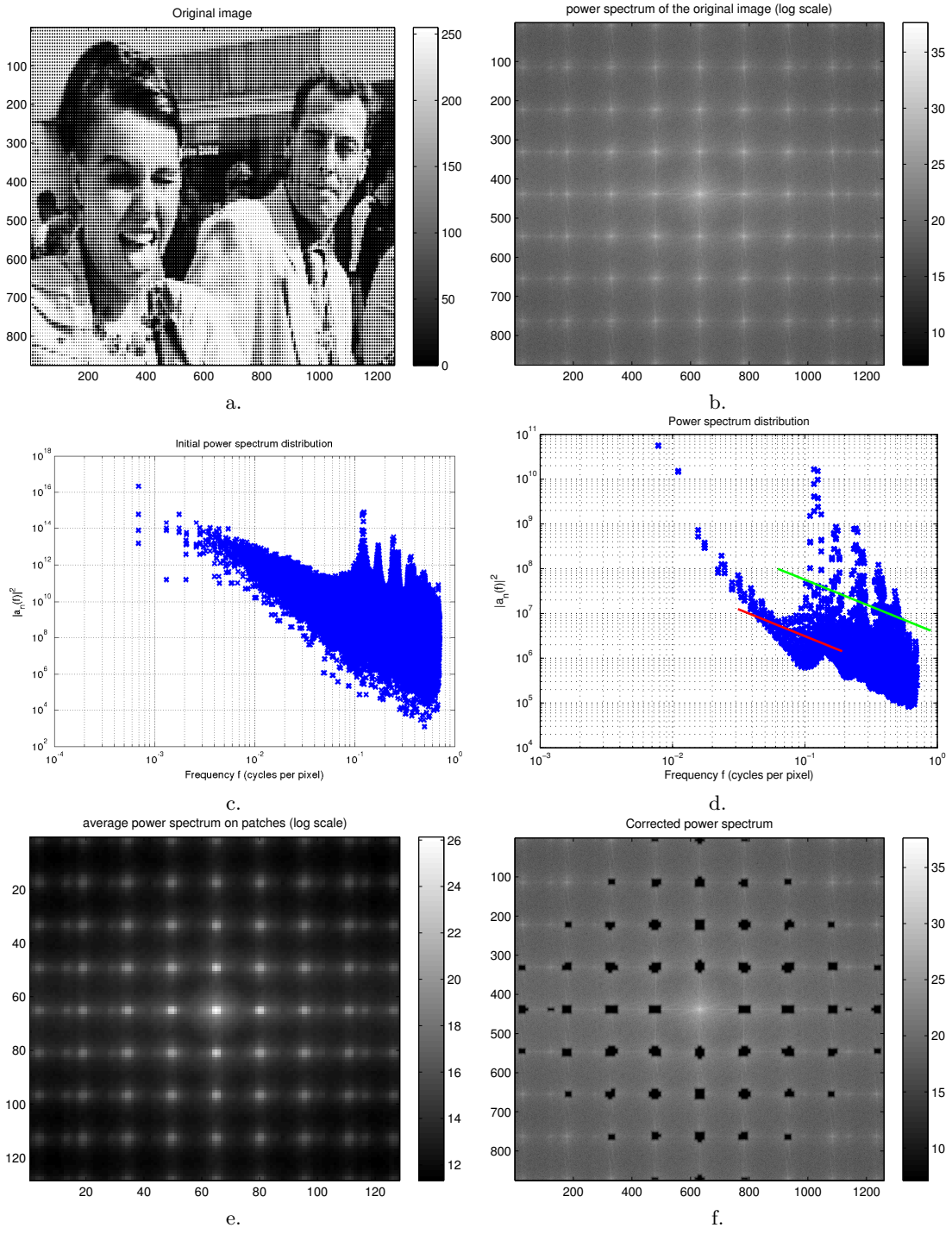

Figure 24: Halftone experiment (9a). a: Noisy image. b: Power spectrum. c: Power spectrum coefficient distribution. d: Average power spectrum distribution. e: Average power spectrum. f: Corrected power spectrum.

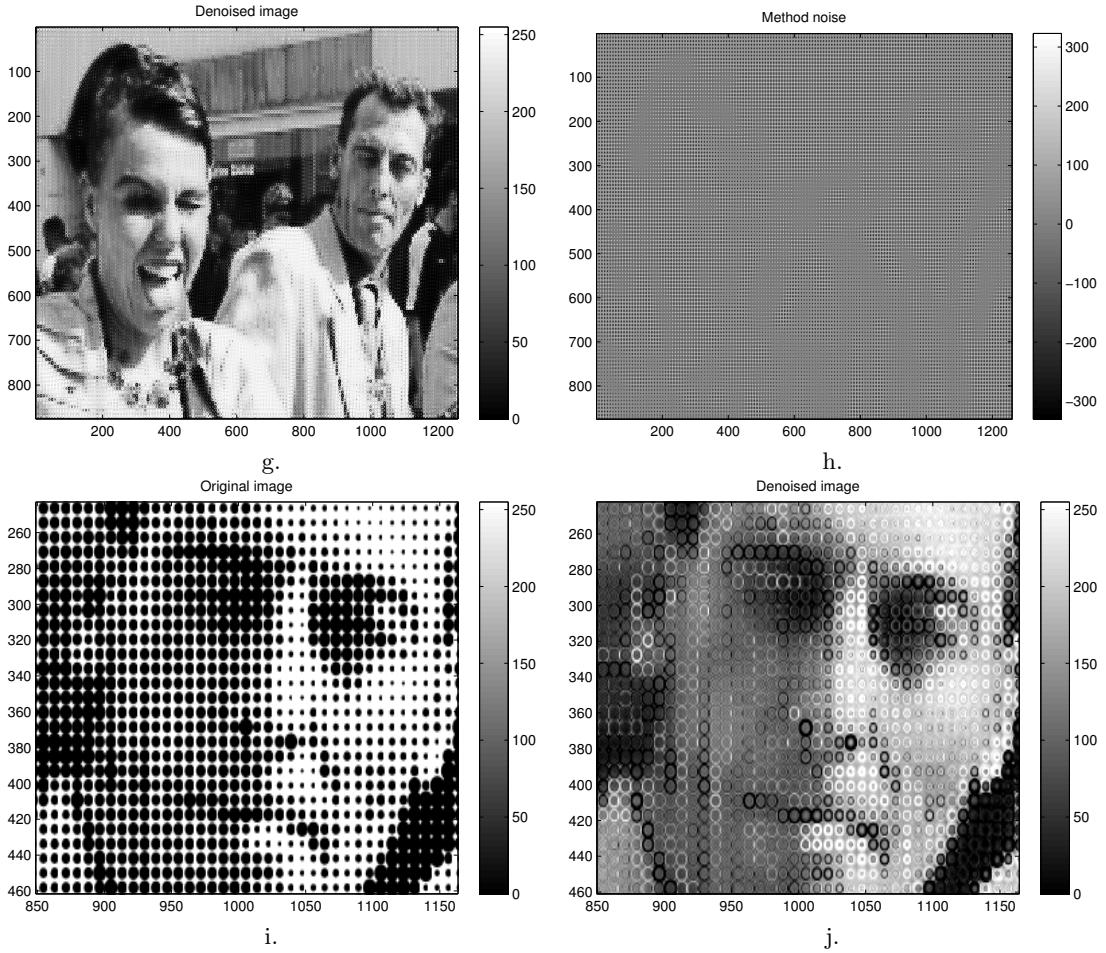

g. h. i. j.

Figure 25: Halftone experiment (9a). g: De-Noised image. h: Estimation of the noise. i: Close-up view of the noisy image. j: Close-up view of the de-noised image.

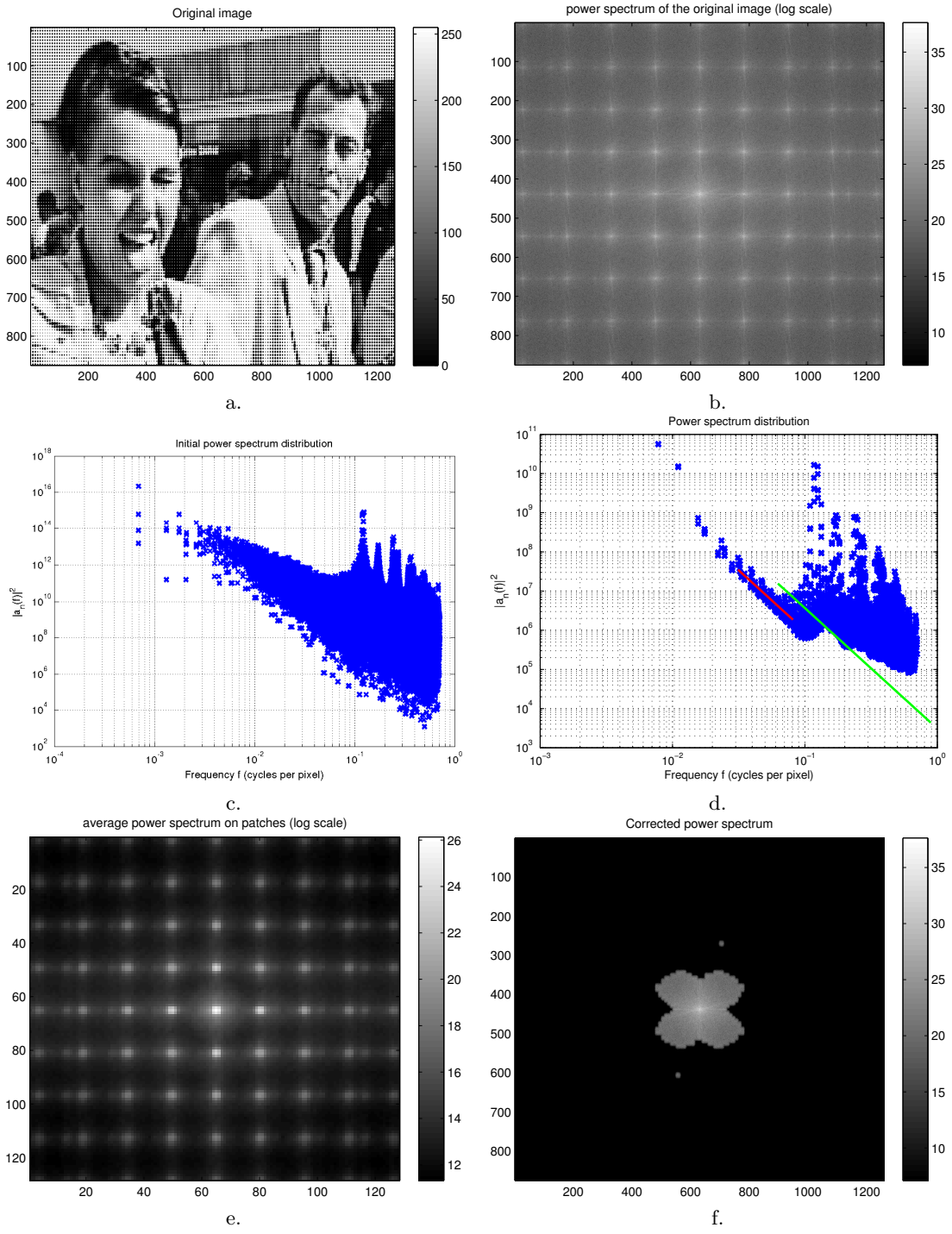

Figure 26: Halftone experiment (9b). a: Noisy image. b: Power spectrum. c: Power spectrum coefficient distribution. d: Average power spectrum distribution. e: Average power spectrum. f: Corrected power spectrum.

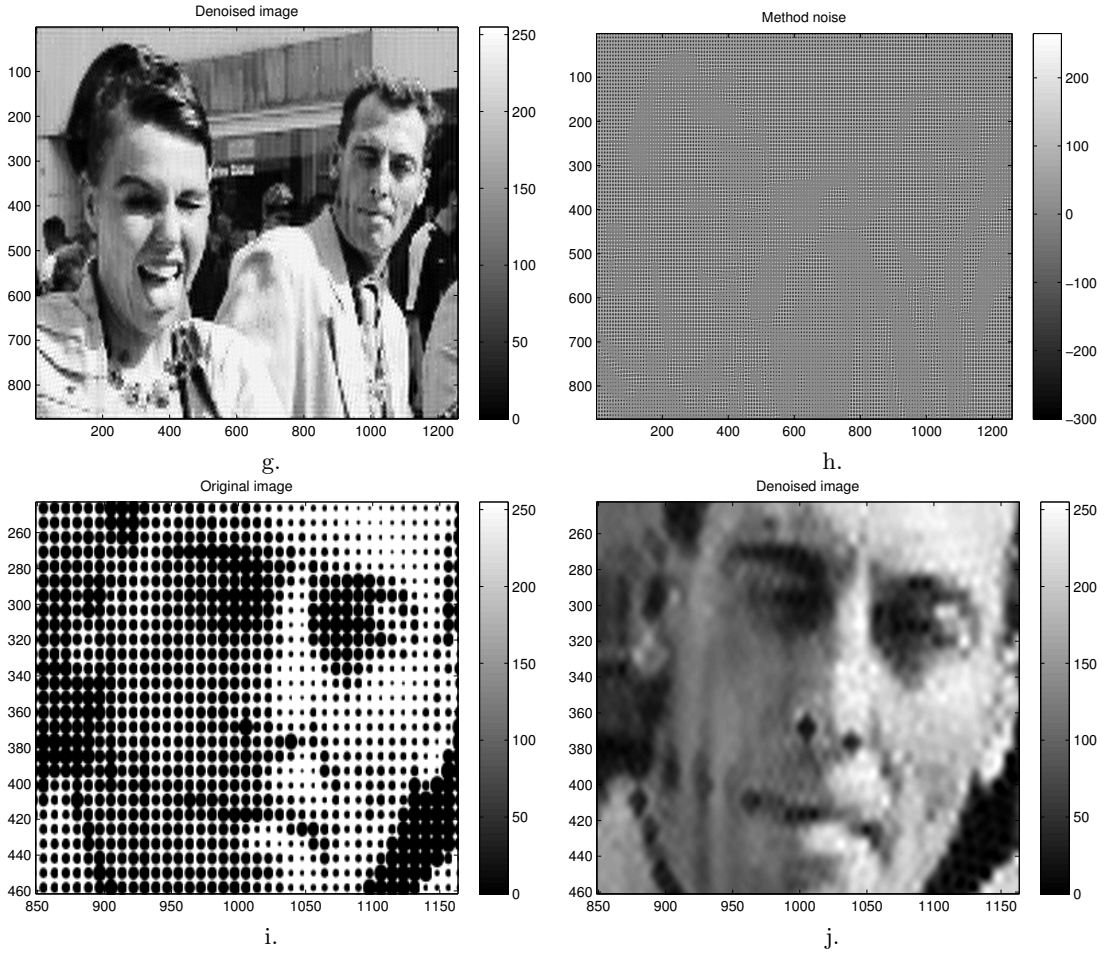

g. h. i. j.

Figure 27: Halftone experiment (9b). g: De-Noised image. h: Estimation of the noise. i: Close-up view of the noisy image. j: Close-up view of the de-noised image.

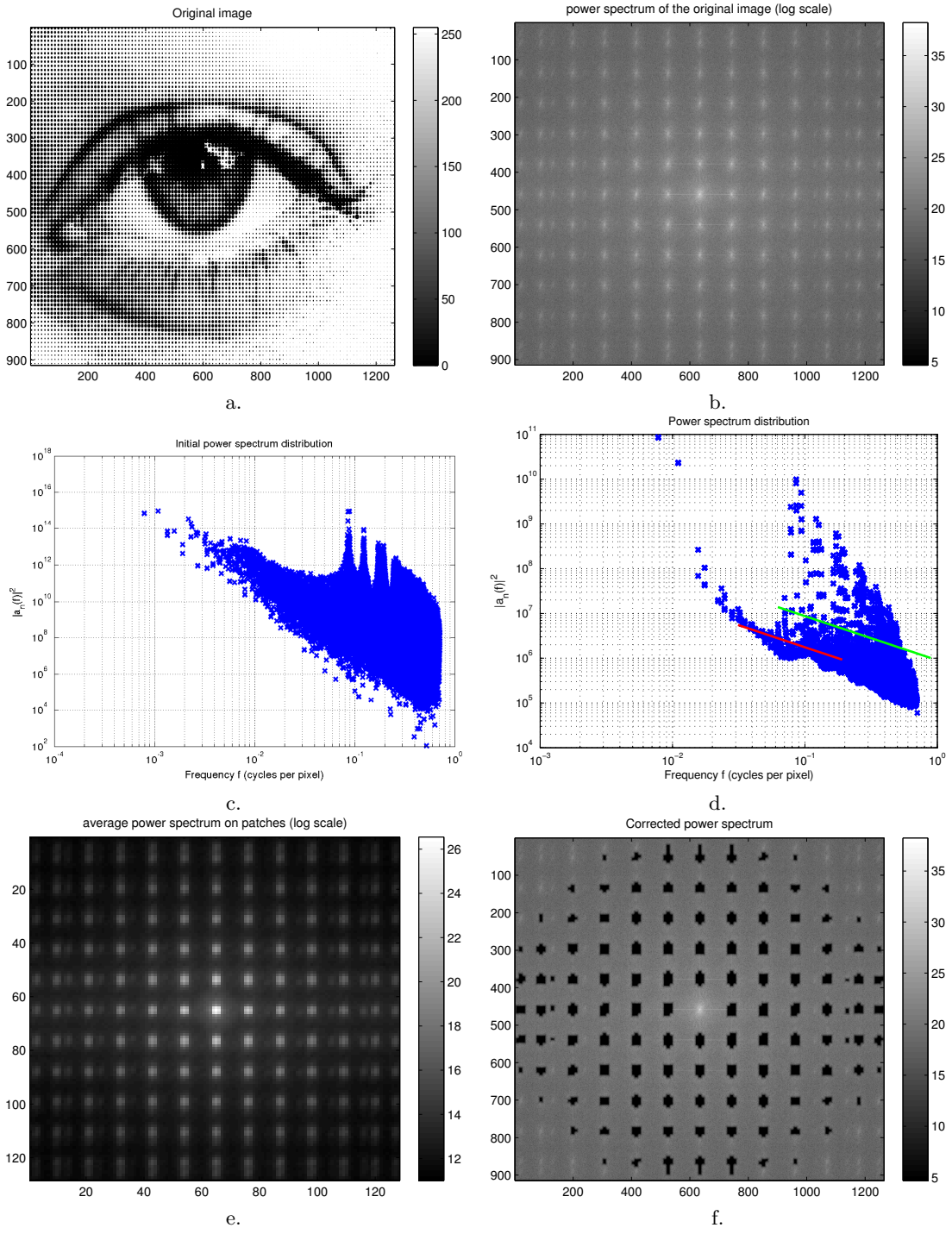

Figure 28: Halftone-eye experiment (10a). a: Noisy image. b: Power spectrum. c: Power spectrum coefficient distribution. d: Average power spectrum distribution. e: Average power spectrum. f: Corrected power spectrum.

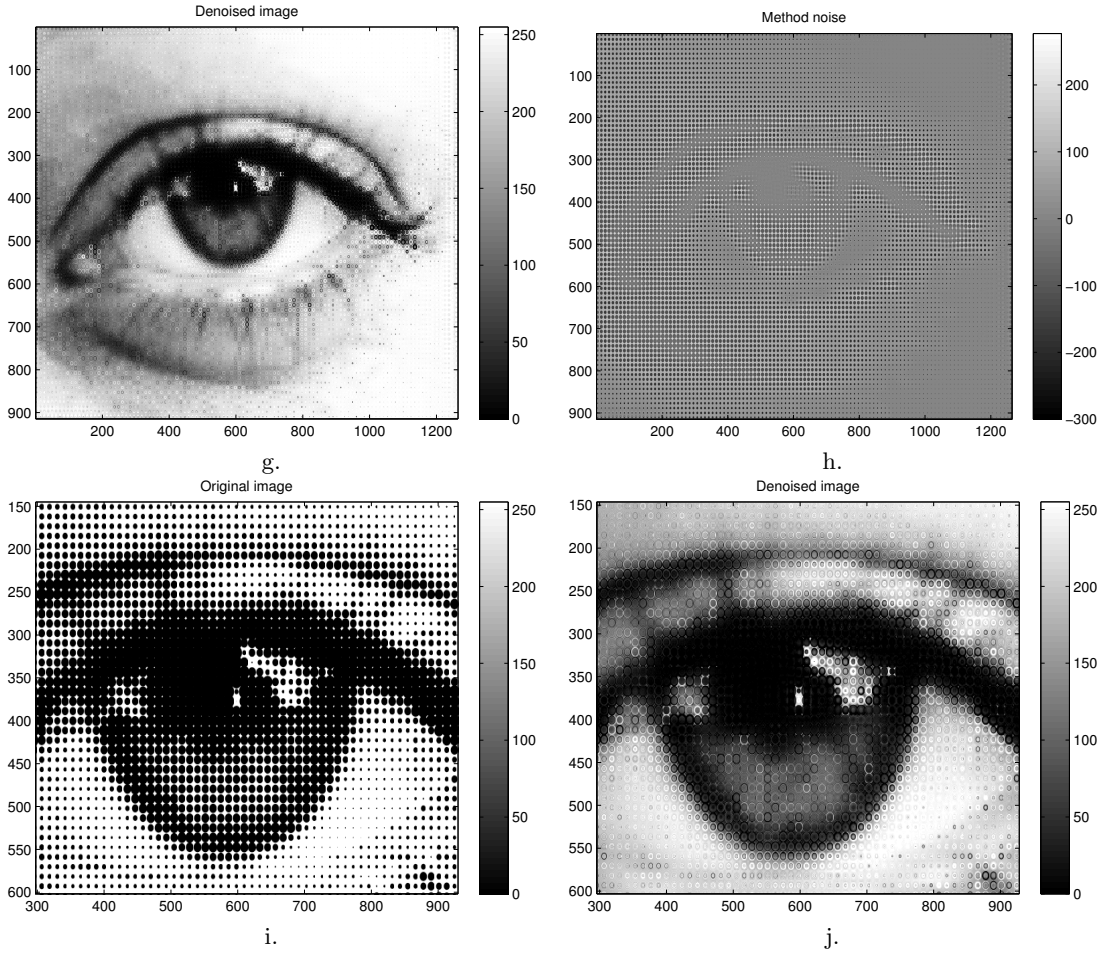

Figure 29: Halftone-eye experiment (10a). g: De-Noised image. h: Estimation of the noise. i: Close-up view of the noisy image. j: Close-up view of the de-noised image.

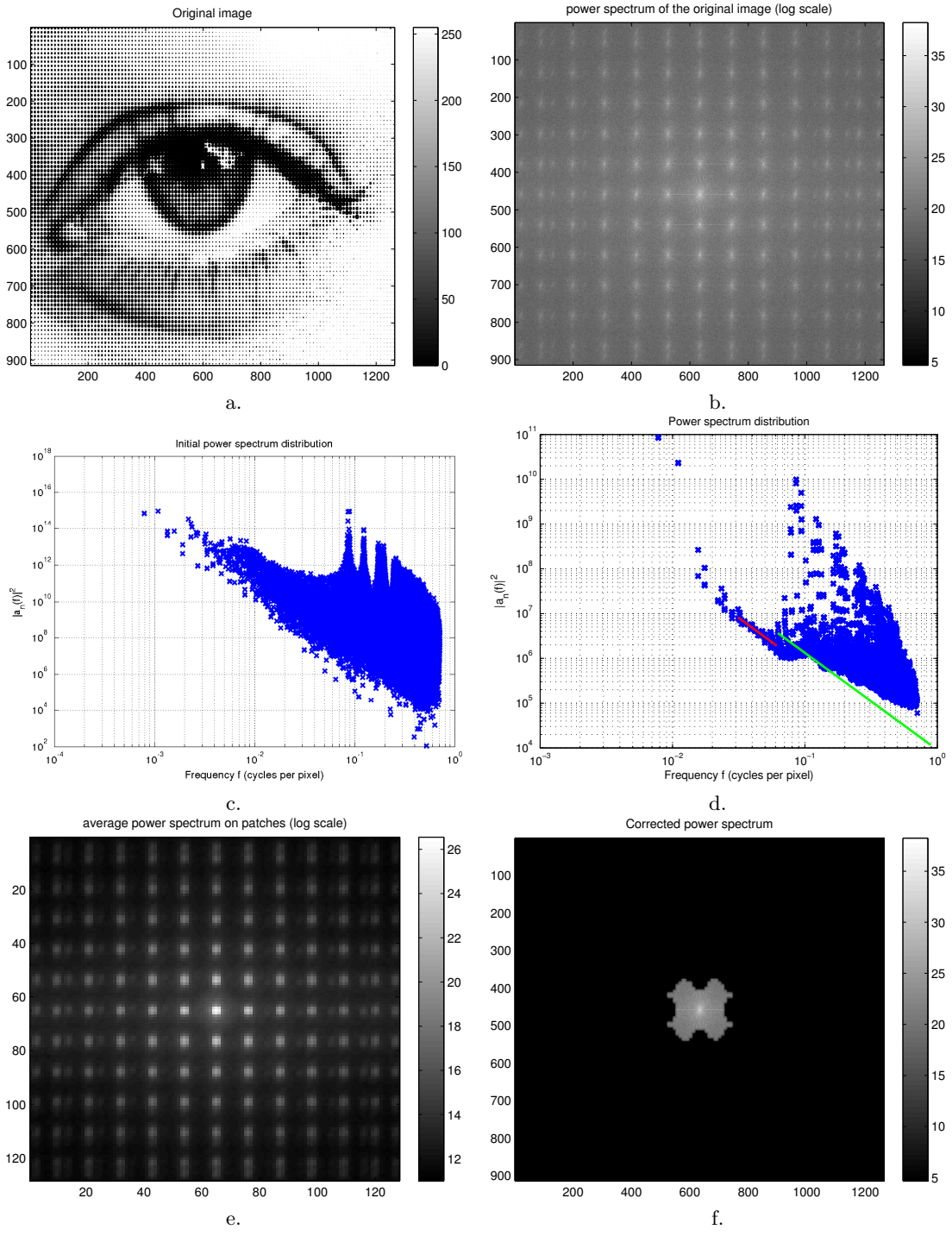

Figure 30: Halftone-eye experiment (10b). a: Noisy image. b: Power spectrum. c: Power spectrum coefficient distribution. d: Average power spectrum distribution. e: Average power spectrum. f: Corrected power spectrum.

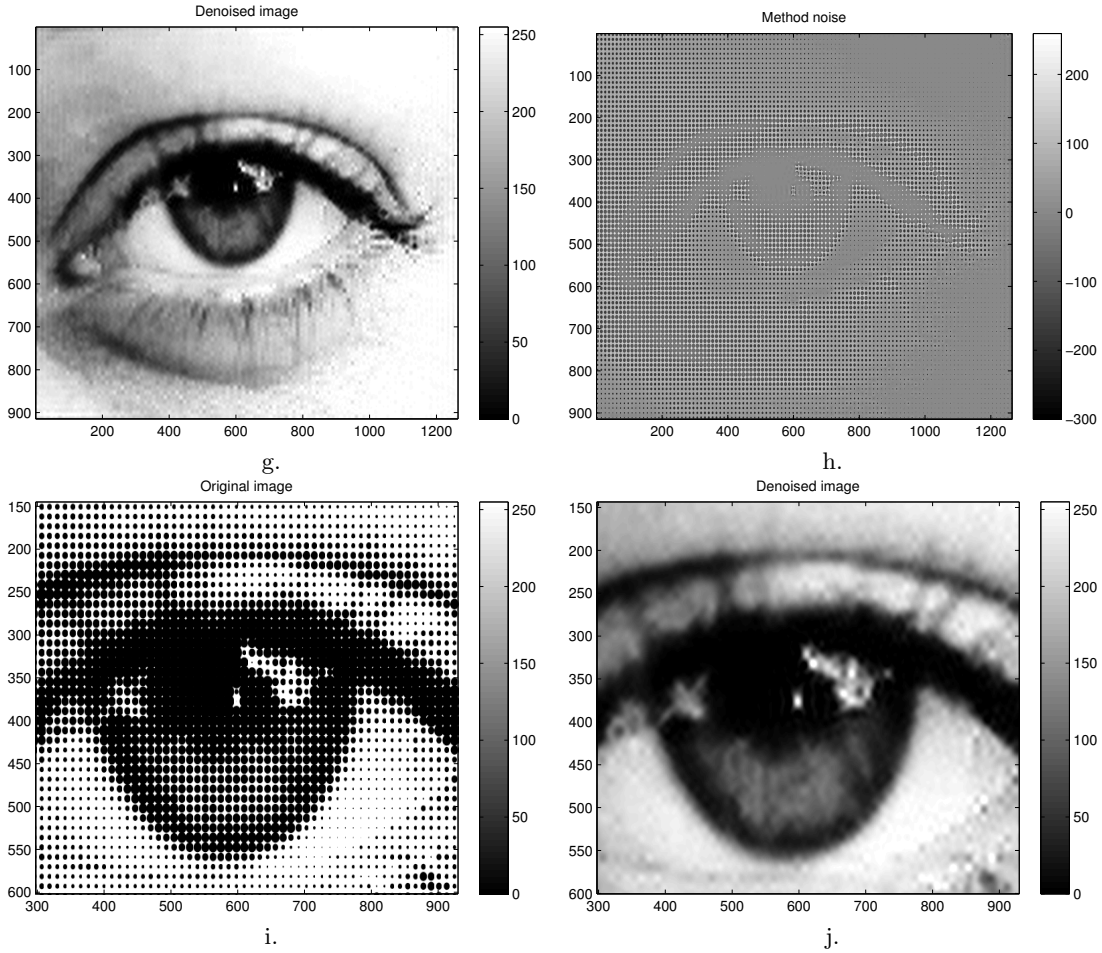

g. h. i. j.

Figure 31: Halftone-eye experiment (10b). g: De-Noised image. h: Estimation of the noise. i: Close-up view of the noisy image. j: Close-up view of the de-noised image.

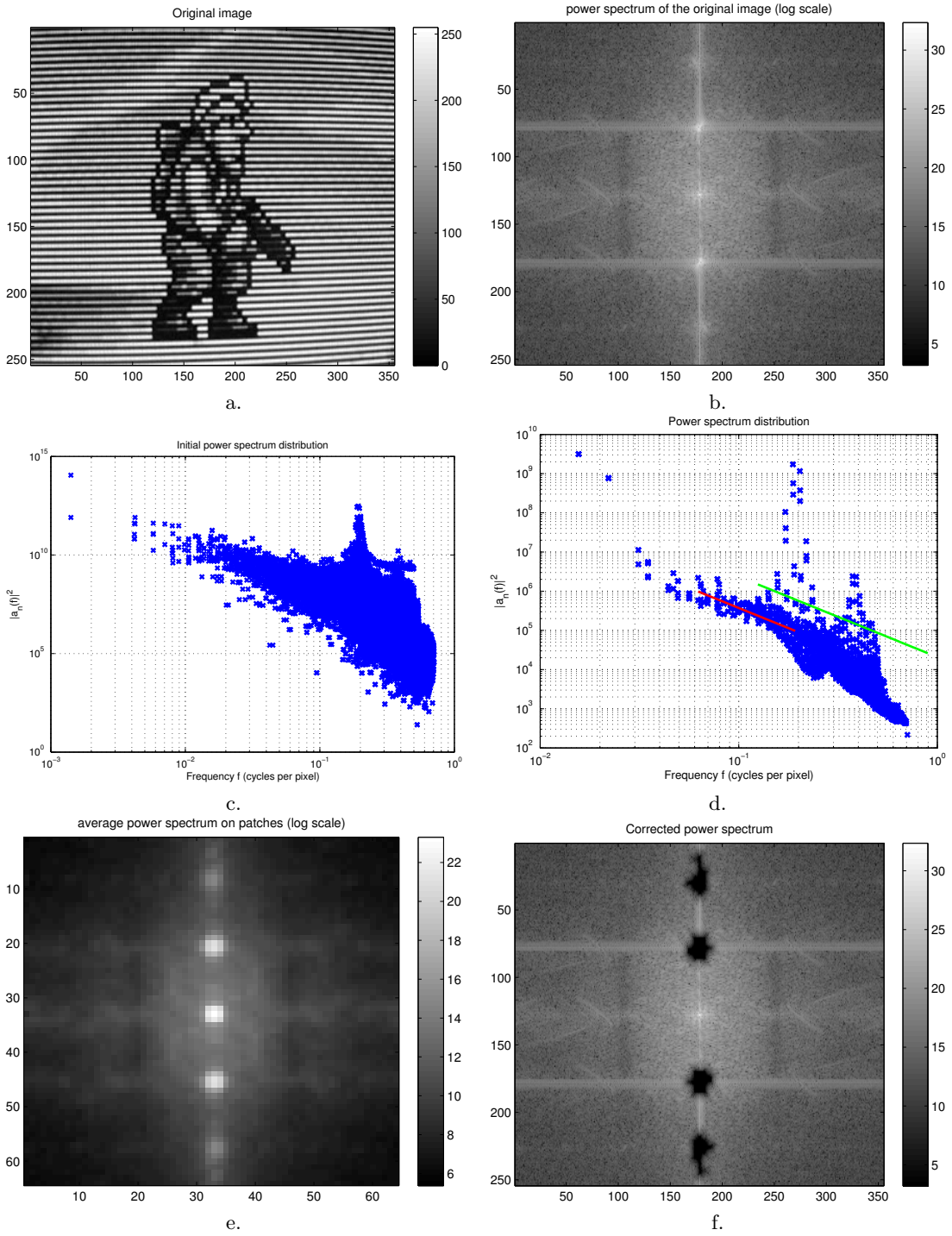

Figure 32: Scanline experiment (11). a: Noisy image. b: Power spectrum. c: Power spectrum coefficient distribution. d: Average power spectrum distribution. e: Average power spectrum. f: Corrected power spectrum.

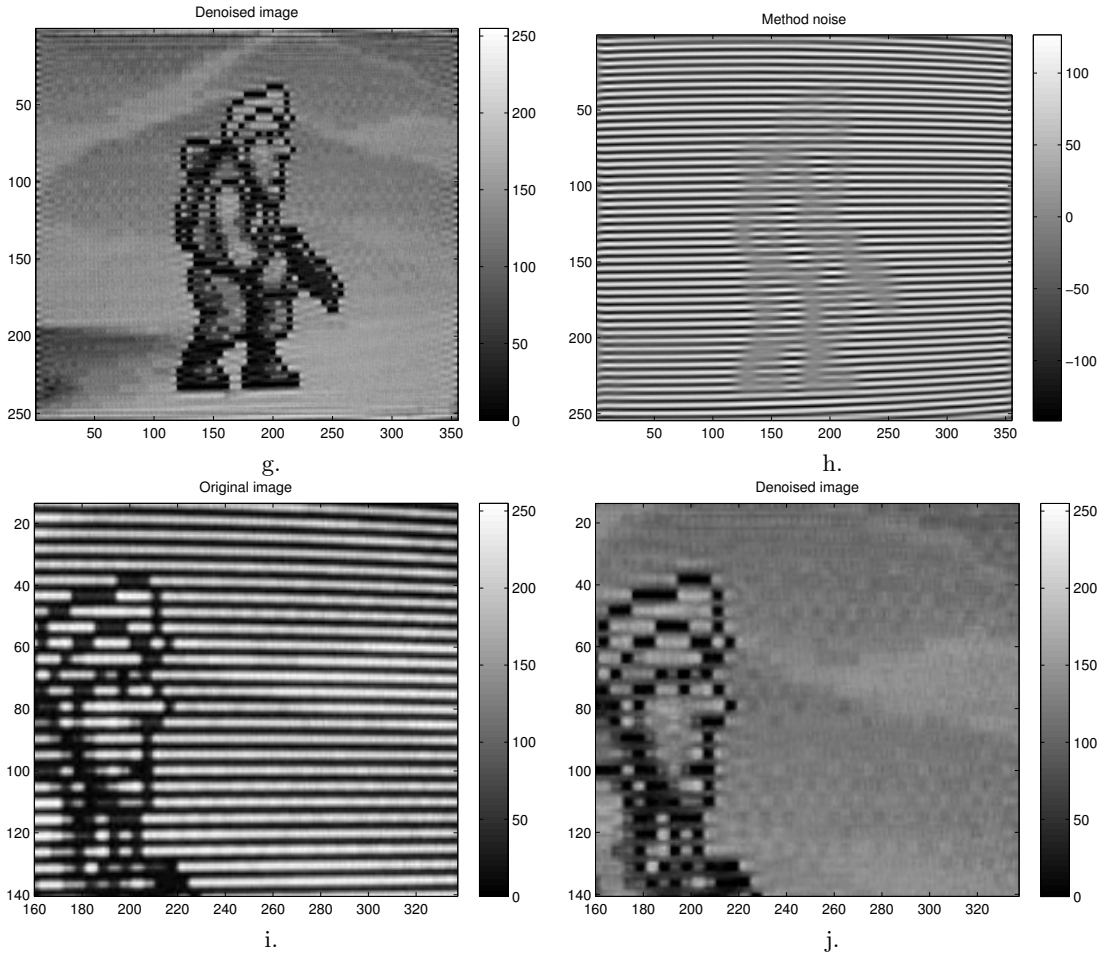

g. h.

i. j.

Figure 33: Scanline experiment (11). g: De-Noised image. h: Estimation of the noise. i: Close-up view of the noisy image. j: Close-up view of the de-noised image.

4.3 A comparison with morphological component analysis

Morphological component analysis (MCA) [8, 23] implements blind source separation by decomposing a linear mixture of several (here two) signals, sparsely represented in morphologically independent basis. Separating the periodic noise and the underlying natural image can be achieved by using a discrete cosine transform (DCT) representation for the periodic noise and a curvelet representation for the image, as suggested in [23].

The results of this decomposition for some of the images of Sec. 4.1 and 4.2 can be found in Figures 34 to 42[1]. The *de-noised image* is the curvelet component, and the *method noise* is the DCT component. Computation times are reported in Table 2.

Even if the parameters would certainly benefit from careful setting, we can see that MCA does not perform as well as the proposed approach. Details of the image can be seen in the method noise (which means that they have been lost from the de-noised image), and some periodic noise can still be seen in the de-noised image. The reason is that the sparsity assumption is probably too optimistic in the problem of interest, as could be expected from the shape of the corresponding notch filter in the Fourier domain. In addition, the retrieved de-noised image appears smoother than with the proposed notch filter. Furthermore, MCA is 150 to 350 times slower than the proposed algorithm, despite the fact that MCA uses compiled functions (our code is native Matlab).

No.	image	time
-	Mandrill (Fig. 34)	30.2
-	Boat (Fig. 35)	30.2
1	Mariner4 (Fig. 36)	136.6
2	Apollo (Fig. 37)	134.3
3	Florida (Fig. 38)	134.4
4	Mariner6 (Fig. 39)	30.4
5	Newspaper (Fig. 40)	134.6
7	Mariner6b (fig. 41)	136.8
11	Scanline (fig. 42)	33.2

Table 2: MCA algorithm: experiment number (as in Sec. 4.2); image name and corresponding figure; computation time (in seconds, Intel Xeon E3-1240 processor).

[1] We use the MCALab software tool:
`https://fadili.users.greyc.fr/demos/WaveRestore/downloads/mcalab/Home.html`
with its default parameters.

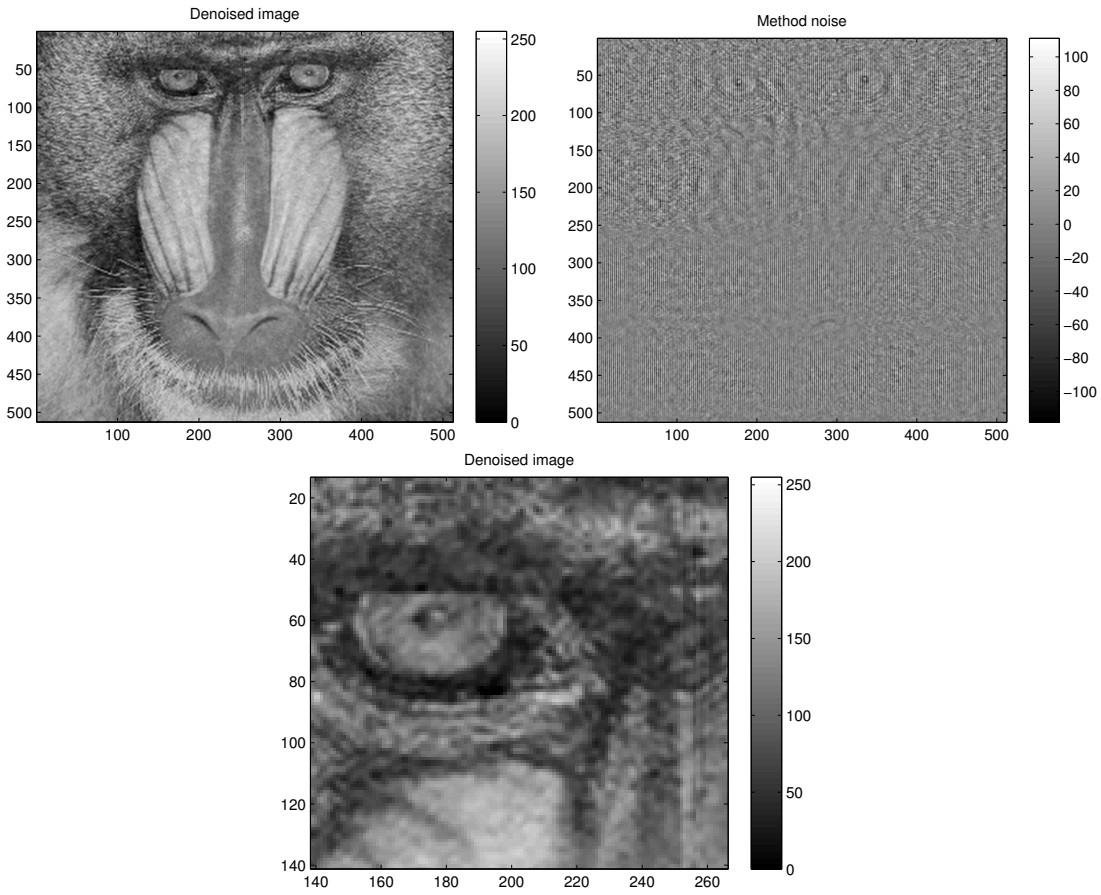

Figure 34: MCA, Mandrill experiment. De-Noised image, periodic noise component, close-up view of the de-noised image. To be compared to Figure 5.

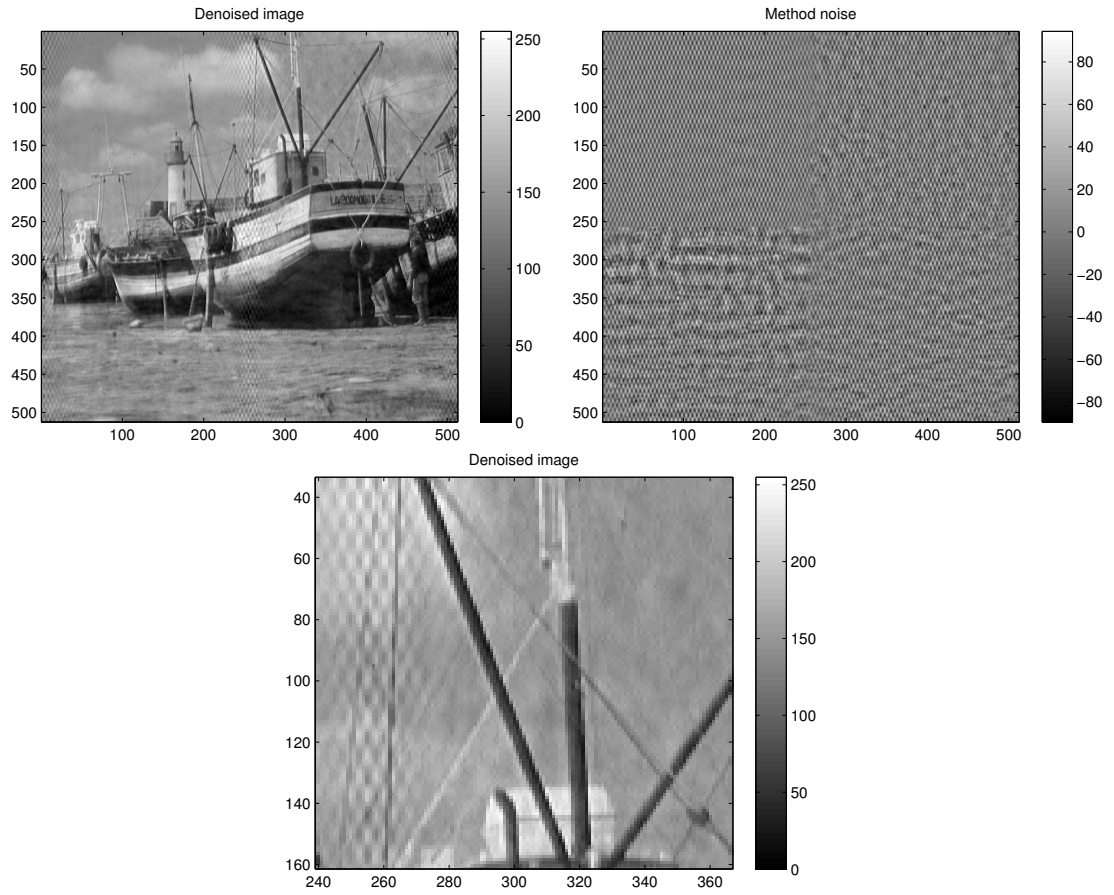

Figure 35: MCA, Boat experiment. De-Noised image, periodic noise component, close-up view of the de-noised image. To be compared to Figure 8.

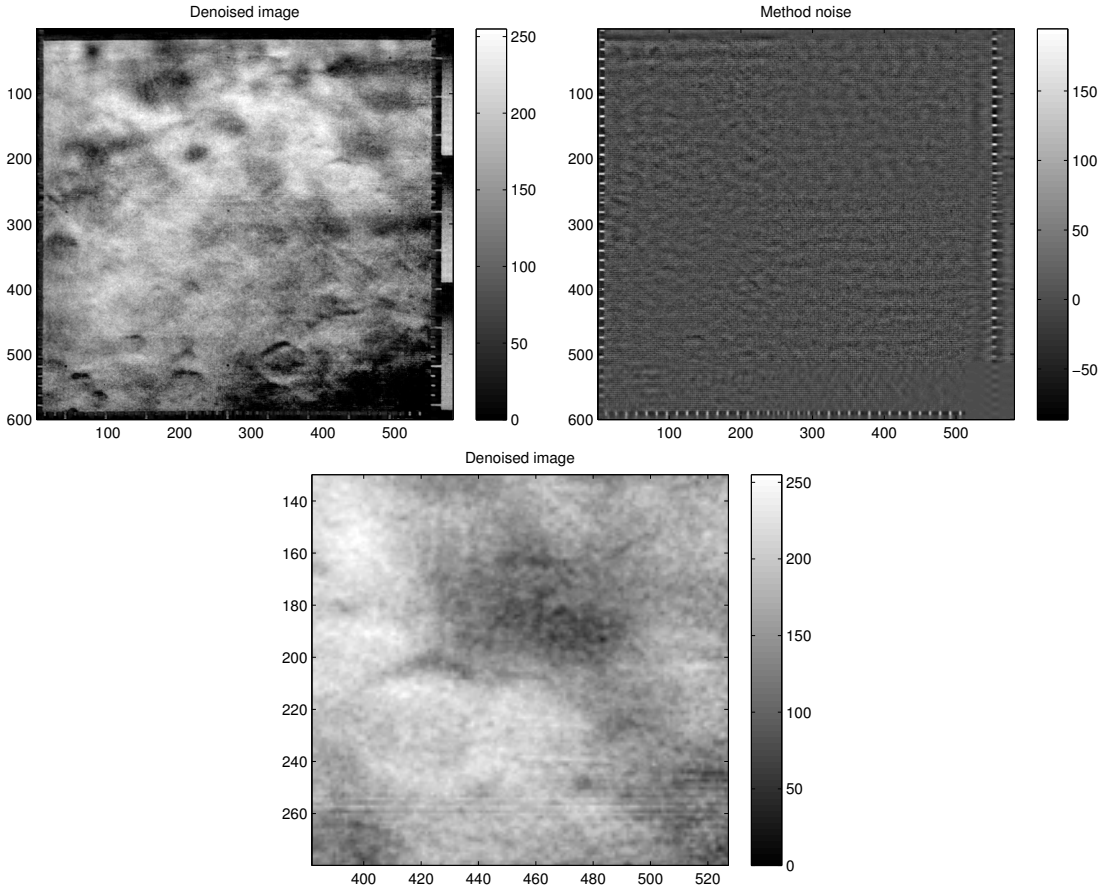

Figure 36: MCA, Mariner4 experiment (1). De-Noised image, periodic noise component, close-up view of the de-noised image. To be compared to Figure 3.

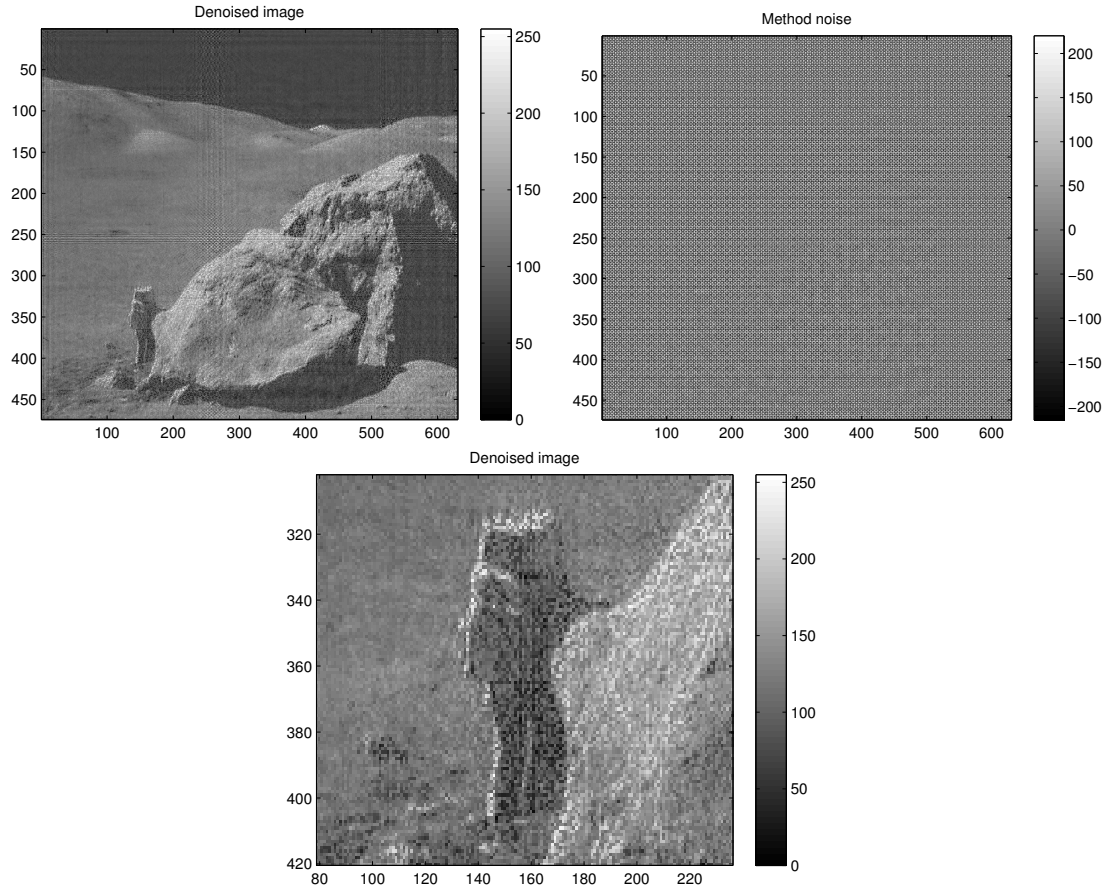

Figure 37: MCA, Apollo experiment (2). De-noised image, periodic noise component, close-up view of the de-noised image. To be compared to Figure 11.

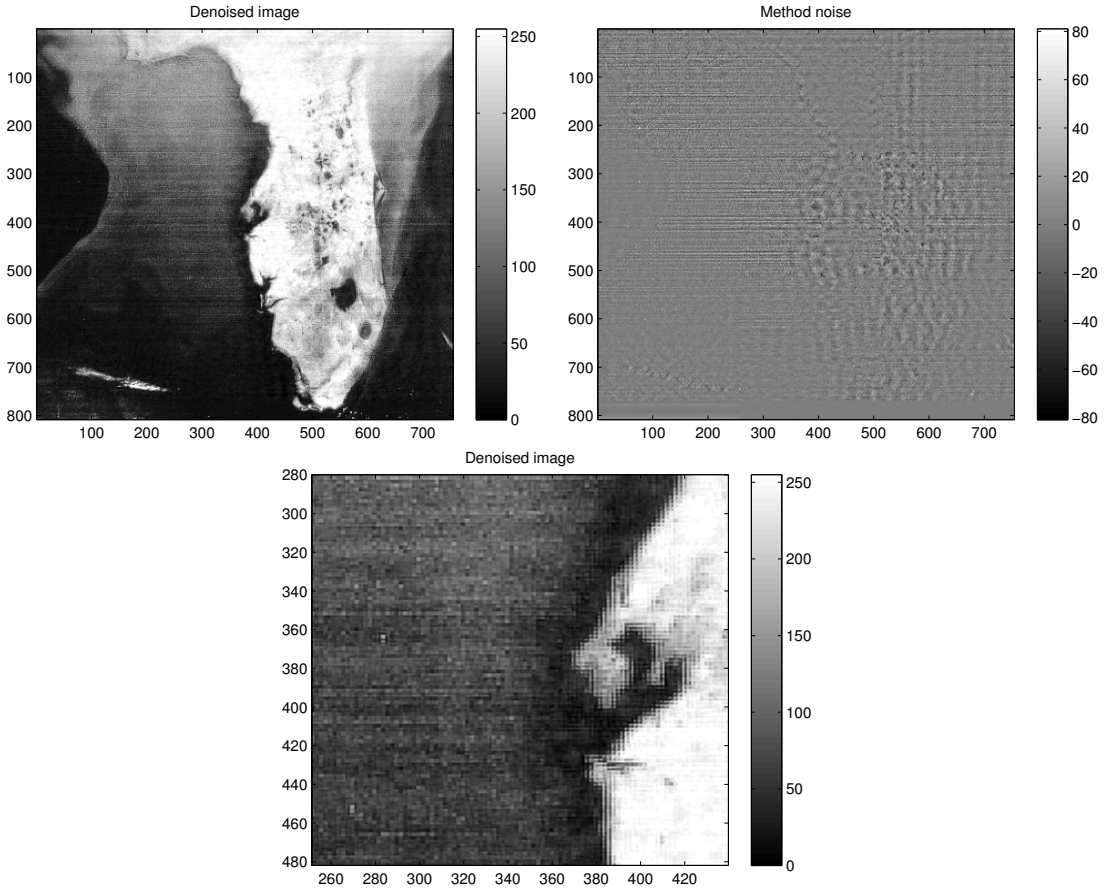

Figure 38: MCA, Florida experiment (3). De-noised image, periodic noise component, close-up view of the de-noised image. To be compared to Figure 13.

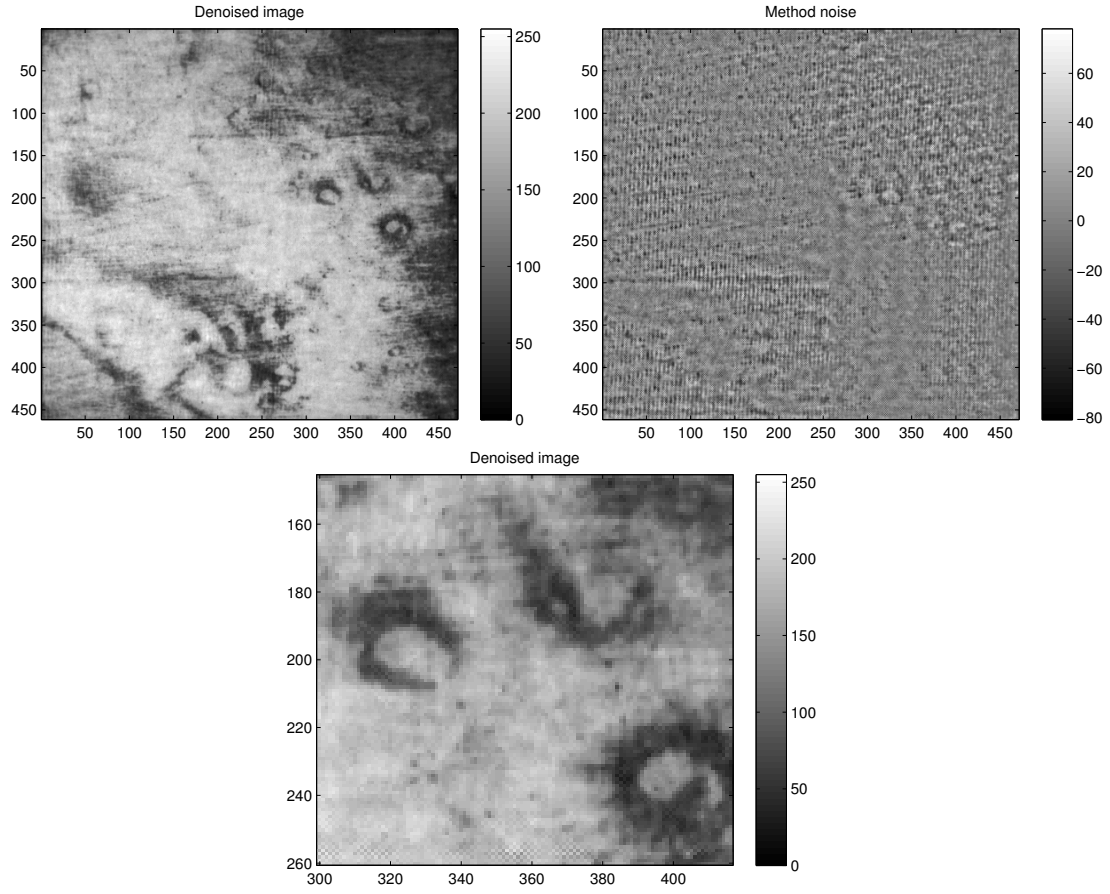

Figure 39: MCA, Mariner6 experiment (4). De-noised image, periodic noise component, close-up view of the de-noised image. To be compared to Figure 15.

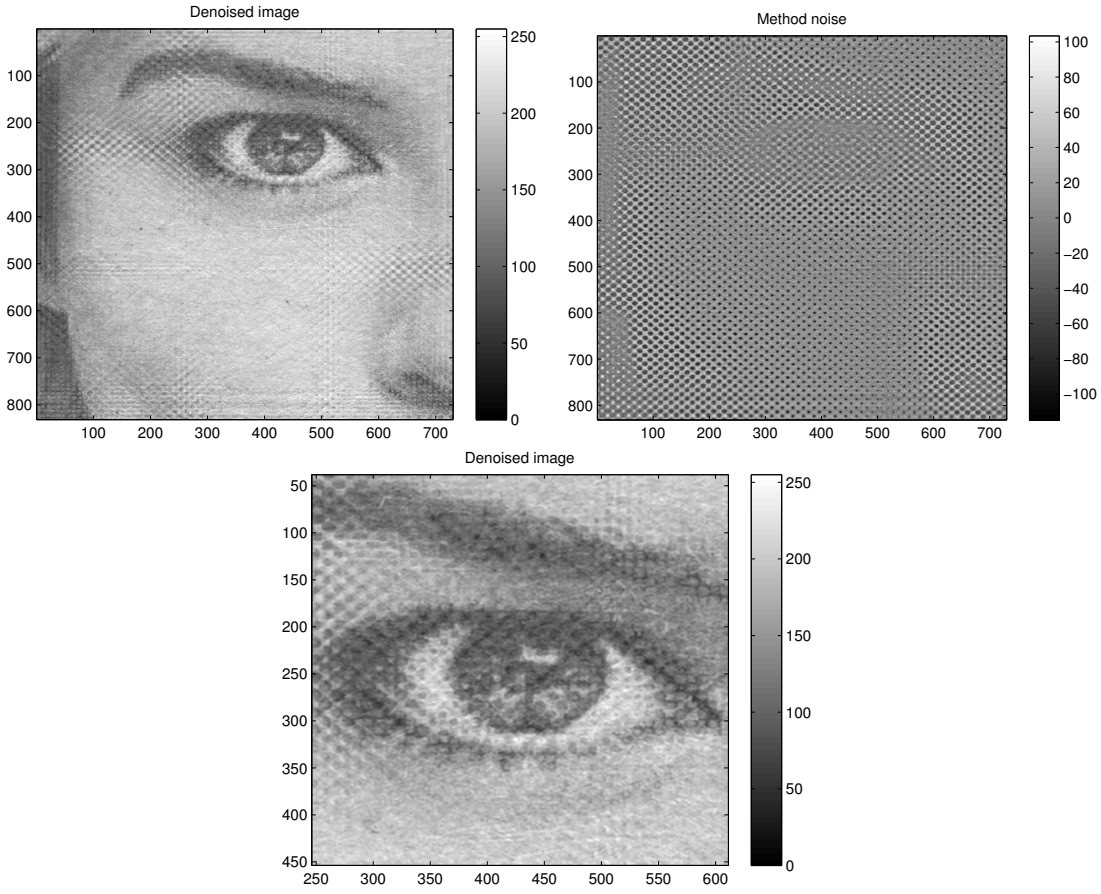

Figure 40: MCA, Newspaper experiment (5). De-noised image, periodic noise component, close-up view of the de-noised image. To be compared to Figure 17.

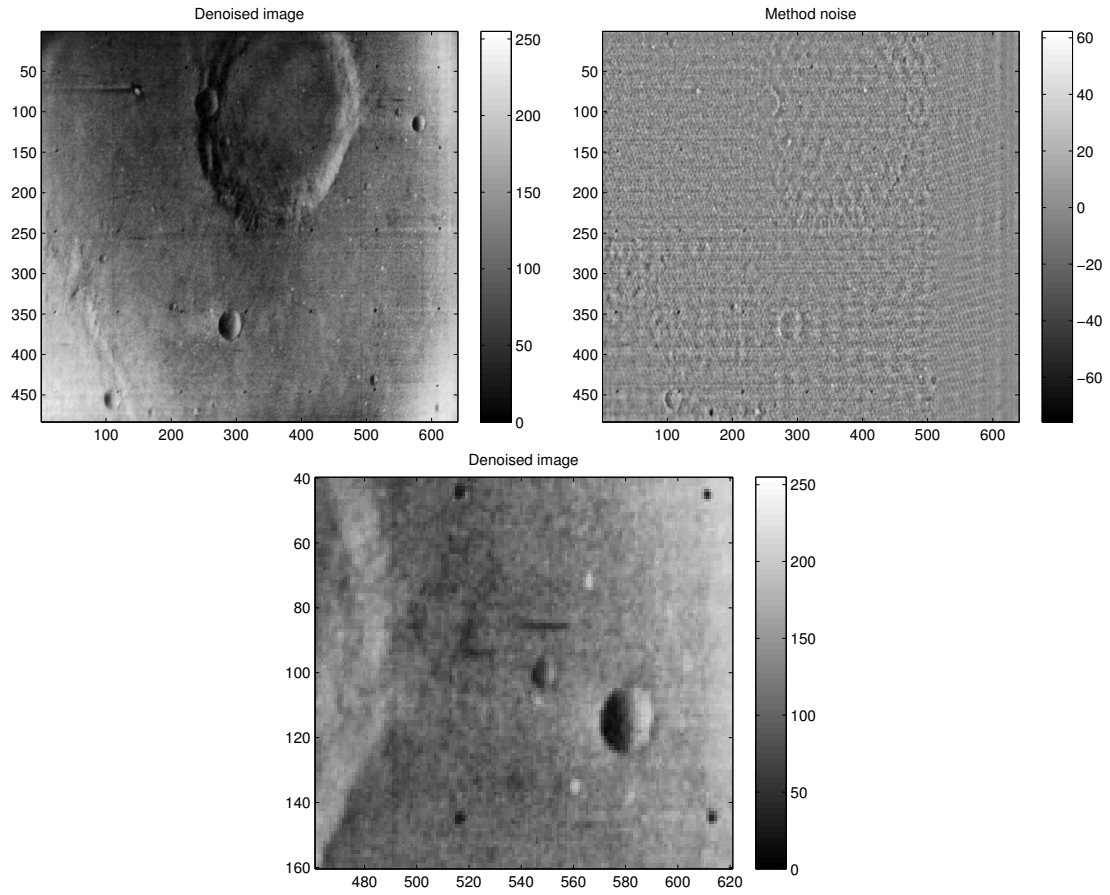

Figure 41: MCA, Mariner6b experiment (7). De-noised image, periodic noise component, close-up view of the de-noised image. To be compared to Figure 21.

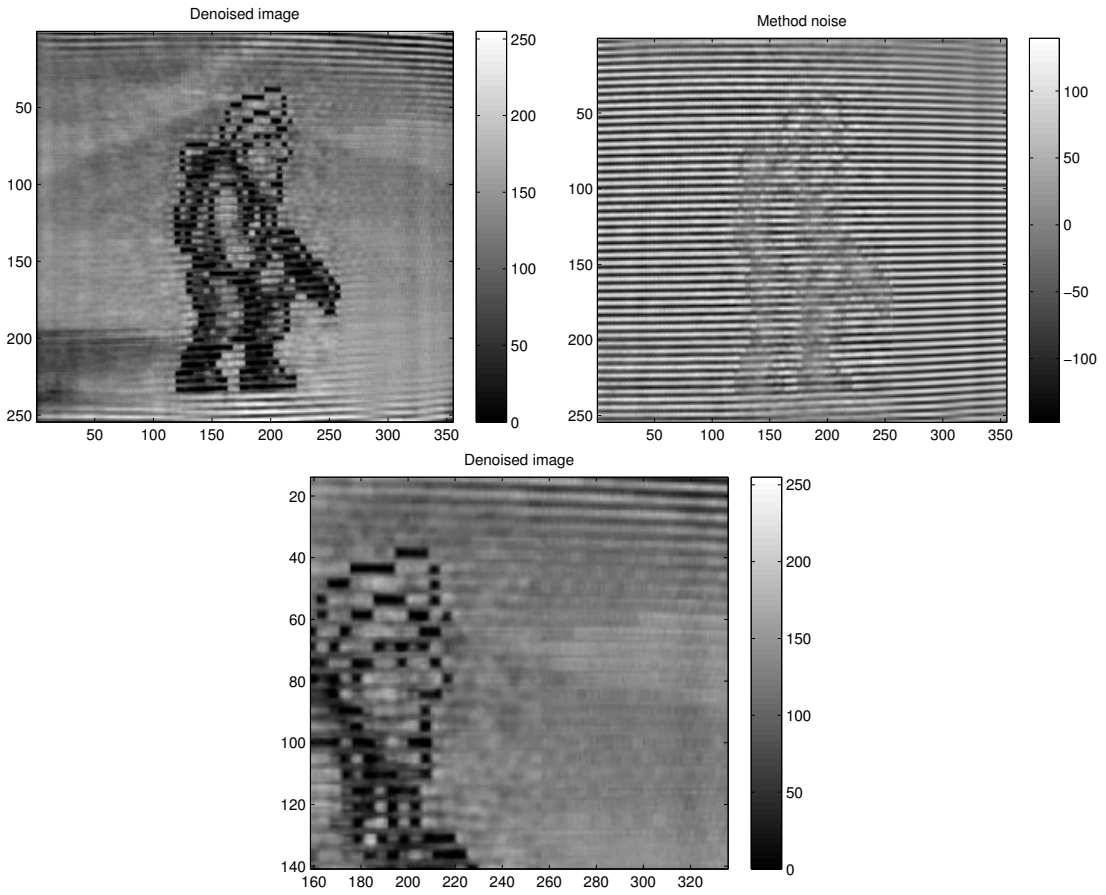

Figure 42: MCA, Scanline experiment (11). De-noised image, periodic noise component, close-up view of the de-noised image. To be compared to Figure 33.

5 Conclusion

This report presents a novel automated approach to pseudo-periodic noise removal in natural images. It is based on the observation that the localization of the Fourier coefficients from the periodic noise are likely to be the only spikes present in the average power spectrum estimated on a set of patches regularly distributed in the image. The corresponding Fourier coefficients are detected as outliers of the power law distribution which is expected from a natural image. This gives an automated notch filter design, which can be used in turn to successfully remove pseudo-periodic noise. The resulting method is limited to "natural" images: this terminology includes remote sensing imaging but not, for example, strain maps in experimental mechanics which, in general, still need a dedicated approach [13]. Aliasing is also potentially detected as pseudo-periodic noise if it affects a large part of the image. Moreover, a comparison shows that the proposed method performs better than a blind source separation algorithm such as MCA. A perspective for this work would be to replace the parametric approach to detecting the spikes caused by noise in the Fourier domain by non-parametric detection such as an a-contrario approach (see, e.g., the books [5, 7]) in the same spirit as in [6].

Acknowledgements. Pr. S. Amziane and Pr. E. Toussaint are gratefully acknowledged for their help in obtaining the strain maps shown in Experiment 6. The authors of MCALab are gratefully acknowledged for making their software library available. This work is partially supported by GdR ISIS (TIMEX project).

References

[1] I. Aizenberg and C. Butakoff. A windowed Gaussian notch filter for quasi-periodic noise removal. *Image and Vision Computing*, 26(10):1347–1353, 2008.

[2] C. Badulescu, M. Grédiac, and J.-D. Mathias. Investigation of the grid method for accurate in-plane strain measurement. *Measurement Science and Technology*, 20(9):095102, 2009.

[3] A. Buades, B. Coll, and J.-M. Morel. A review of image denoising algorithms, with a new one. *SIAM Journal on Multiscale Modeling and Simulation*, 4(2):490–530, 2005.

[4] M. Cannon, A. Lehar, and F. Preston. Background pattern removal by power spectral filtering. *Applied Optics*, 22(6):777–779, 1983.

[5] F. Cao, J.L. Lisani, J.-M. Morel, P. Musé, and F. Sur. *A theory of shape identification*. Number 1948 in Lecture Notes in Mathematics. Springer, 2008.

[6] B. Coulange and L. Moisan. An aliasing detection algorithm based on suspicious colocalizations of Fourier coefficients. In *Proceedings of the IEEE International Conference on Image Processing (ICIP)*, pages 2013–2016, Hong Kong, 2010.

[7] A. Desolneux, L. Moisan, and J.-M. Morel. *From Gestalt theory to image analysis: a probabilistic approach*. Interdisciplinary applied mathematics. Springer, 2008.

[8] M.J. Fadili, J.-L. Starck, J. Bobin, and Y. Moudden. Image decomposition and separation using sparse representations: An overview. *Proceedings of the IEEE*, 98(6):983–994, 2010.

[9] J. Fehrenbach, P. Weiss, and C. Lorenzo. Variational algorithms to remove stationary noise: Applications to microscopy imaging. *IEEE Transactions on Image Processing*, 21(10):4420–4430, 2012.

[10] D.J. Field. Relations between the statistics of natural images and the response properties of cortical cells. *Journal of the Optical Society of America, A*, 4:2379–2394, 1987.

[11] R.C. Gonzalez and R.E. Woods. *Digital Image Processing (3rd Edition)*. Prentice-Hall, 2006.

[12] M. Grédiac, F. Sur, C. Badulescu, and J.-D. Mathias. Using deconvolution to improve the metrological performance of the grid method. *Optics and Lasers in Engineering*, 51(6):716–734, 2013.

[13] M. Grédiac, F. Sur, and B. Blaysat. Removing quasi-periodic noise in strain maps by filtering in the Fourier domain. 2015. Submitted for publication.

[14] G.A.A. Hudhud and M.J. Turner. Digital removal of power frequency artifacts using a Fourier space median filter. *IEEE Signal Processing Letters*, 12(8):573–576, 2005.

[15] A. Hyvärinen, J. Hurri, and P.O. Hoyer. *Natural Image Statistics: A Probabilistic Approach to Early Computational Vision.* Springer, 2009.

[16] K. Jalalzai. *Regularization of inverse problems in image processing.* PhD thesis, École Polytechnique, Palaiseau, France, 2012.

[17] M. Lebrun, M. Colom, A. Buades, and J.-M. Morel. Secrets of image denoising cuisine. *Acta Numerica*, 21(1):475–576, 2012.

[18] P. Milanfar. A tour of modern image filtering: New insights and methods, both practical and theoretical. *IEEE Signal Processing Magazine*, 30(1):106–128, 2013.

[19] A. Oliva and A. Torralba. Modeling the shape of the scene: A holistic representation of the spatial envelope. *International Journal of Computer Vision*, 42(3):145–175, 2001.

[20] T. C. Rindfleisch, J. A. Dunne, H. J. Frieden, W. D. Stromberg, and R. M. Ruiz. Digital processing of the Mariner 6 and 7 pictures. *Journal of Geophysical Research*, 76(2):394–417, 1971.

[21] R.A. Schowengerdt. *Remote sensing: models and methods for image processing.* Academic Press, 2006.

[22] R. Srinivasan, M. Cannon, and J. White. Landsat data destriping using power spectral filtering. *Optical Engineering*, 27(11):939–943, 1988.

[23] J.-L. Starck, M. Elad, and D.L. Donoho. Image decomposition via the combination of sparse representations and a variational approach. *IEEE Transactions on Image Processing*, 14(10):1570–1582, 2005.

[24] F. Sur and M. Grédiac. Towards deconvolution to enhance the grid method for in-plane strain measurement. *AIMS Inverse Problems and Imaging*, 8(1):259–291, 2014.

[25] F. Sur and M. Grédiac. Automated removal of quasi-periodic noise using frequency domain statistics. *IS&T / SPIE Journal of Electronic Imaging*, 2015. To be published.

[26] A. Torralba and A. Oliva. Statistics of natural image categories. *Network*, 14(3):391–412, 2003.

[27] A. van der Schaaf and J.H. van Hateren. Modelling the power spectra of natural images: Statistics and information. *Vision Research*, 36(17):2759–2770, 1996.

[28] M. Zibulevsky and B.A. Pearlmutter. Blind source separation by sparse decomposition in a signal dictionary. *Neural Computation*, 13(4):863–882, 2001.

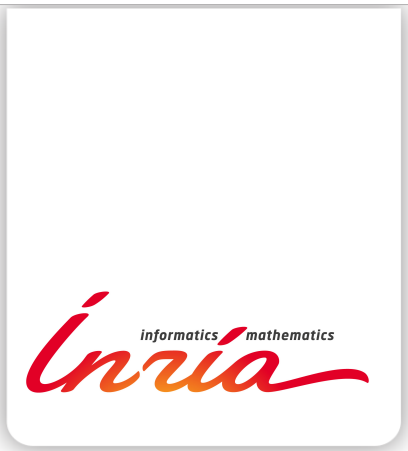

RESEARCH CENTRE
NANCY – GRAND EST

615 rue du Jardin Botanique
CS20101
54603 Villers-lès-Nancy Cedex

Publisher
Inria
Domaine de Voluceau - Rocquencourt
BP 105 - 78153 Le Chesnay Cedex
inria.fr

ISSN 0249-6399